The Astrophysical Journal Letters, 941:L11 (15pp), 2022 December 10 https://doi.org/10.3847/2041-8213/aca1bf

What Are Those Tiny Things? A First Study of Compact Star Clusters in the SMACS0723 Field with JWST

Andreas L. Faisst[1], Ranga Ram Chary[1], Gabriel Brammer[2,3], and Sune Toft[2,3]

[1] Caltech/IPAC, MS314-6, 1200 E. California Boulevard, Pasadena, CA 91125, USA; afaisst@ipac.caltech.edu

[2] Cosmic Dawn Center (DAWN), Copenhagen, Denmark

[3] Niels Bohr Institute, University of Copenhagen, Jagtvej 128, D-2200 Copenhagen, Denmark

Received 2022 August 10; revised 2022 November 6; accepted 2022 November 10; published 2022 December 8

Abstract

We use the unprecedented resolution and depth of the JWST NIRCam Early Release Observations at 1–5 μm to study the stellar mass, age, and metallicity of compact star clusters in the neighborhood of the host galaxies in the SMACS J0723.3–7327 galaxy cluster field at $z = 0.39$. The measured colors of these star clusters show a similar distribution as quiescent galaxies at the same redshift, but are >3 mag fainter than the current depths of wide-field galaxy survey. The star clusters are unresolved in the NIRCam/F150W data suggesting sizes smaller than 50 pc. This is significantly smaller than star-forming clumps or dwarf galaxies in local galaxies. From fitting their photometry with simple stellar population (SSP) models, we find stellar metallicities consistent with 0.2–0.3 $Z_\odot$ and ages of $1.5^{+0.5}_{-0.5}$ Gyr. We rule out metallicities $<0.2\,Z_\odot$ and solar/supersolar at 4σ significance. Assuming mass-to-light ratios obtained from the best-fit SSP, we estimate stellar masses of $2.4^{+3.0}_{-1.5} \times 10^6\,M_\odot$. These are between average masses of local globular clusters and dwarf galaxies. Our analysis suggests middle-aged globular cluster with relatively recent formation times at $z = 0.5$–0.7, which could have been subsequently stripped away from their host galaxies due to interactions in the cluster environment or formed in cold flows onto the cluster core. However, we cannot rule out these objects being compact cores of stripped dwarf galaxies.

Unified Astronomy Thesaurus concepts: Globular star clusters (656); Galaxy clusters (584); Stellar populations (1622); Metallicity (1031); Galaxy formation (595); Dwarf galaxies (416)

1. Introduction

The Early Release Observations (ERO; Pontoppidan et al. 2022) have already showcased the capabilities of the new James Webb Space Telescope (JWST; Rigby et al. 2022) in terms of its sensitivity and resolution at near-infrared wavelengths.

Here, we use the unprecedented sensitivity of the JWST ERO data to study for the first time, the faintest and most compact structures around the galaxies associated with the SMACS J0723.3–7327 galaxy cluster field (hereafter SMACS0723) at $z = 0.39$. Although these objects appear to be consistent with compact star clusters (or globular clusters), they could just as well be the cores of stripped dwarf galaxies.

Globulars around galaxies are abundant and have been observed in our Milky Way as well as many local galaxies (e.g., Harris & Racine 1979; Larsen et al. 2001; Brodie et al. 2014; Harris et al. 2014; Massari et al. 2019). The number of globular cluster hosted by galaxies range from a few to tens for dwarf galaxies such as the Magellanic Clouds (e.g., Georgiev et al. 2010), to a few hundreds for intermediate-mass galaxies such as our Milky Way or M31 (e.g., Harris 1991; Massari et al. 2019), to thousands and more for massive brightest cluster galaxies (BCGs) in galaxy clusters (e.g., Peng et al. 2008; Alamo-Martínez et al. 2013; Harris et al. 2017), which early on were also associated with the intercluster medium (ICM; e.g., Bassino et al. 2003; Jordán et al. 2003).

There are different mechanisms suggested for the formation of a globular cluster. Old globular clusters, among the oldest stellar structures in our universe (e.g., Ricotti et al. 2016), could be formed through rapid processes (such as the collapse of gas clouds; e.g., Peebles & Dicke 1968; Forbes et al. 2018) in the early stages of the universe (such as the Epoch of Reionization at $z \sim 6$). On the other hand, the peak formation of globular cluster (i.e., their ages) may coincide with the peak of cosmic star formation density in galaxies around $z \sim 2$, suggesting they are formed via continuous star formation in gas-rich environments (Harris 1991; Brodie & Strader 2006; Forbes et al. 2018). Indeed, some observations have suggested such a scenario by finding young globular cluster in dense, gas-rich merging systems (Schweizer & Seitzer 1998; de Grijs et al. 2001; Trujillo-Gomez et al. 2021) and current theoretical models mostly assume such a coevolutionary scenario (e.g., Pfeffer et al. 2018; Choksi & Gnedin 2019; El-Badry et al. 2019; Li & Gnedin 2019). There are also observational hints of cluster formation from cooled gas from the ICM to the galaxy cluster core (e.g., Holtzman et al. 1992). For an in-depth discussion of the different globular cluster formation mechanisms, we refer the readers to Kruijssen (2015).

Age determination based on main-sequence turnoff from colors of single stars and cooling curves from long-lived white dwarfs suggest a dominant population of very old globular clusters with a range of metallicity as well as a "young" branch for which metallicity is anticorrelated with age (Harris & Racine 1979; Krauss & Chaboyer 2003; Marín-Franch et al. 2009; Forbes & Bridges 2010; Leaman et al. 2013; VandenBerg et al. 2013; Forbes et al. 2015, 2018; Kruijssen et al. 2019; Massari et al. 2019). The latter may be associated with disruption events of dwarf galaxies and accretion (in situ versus ex situ formation; see also Kruijssen et al. 2019). Among the young globular clusters, the metal-poor population is slightly older than the metal-rich population (12.5 versus 11.5 Gyr; Forbes et al. 2018); however, these differences are of low significance due to uncertainties in the age measurements. Similarly, the absolute ages of the oldest and most metal-poor globular clusters have a significant range. Alternative age measurements by Forbes et al. (2015) (assuming that the metallicity of globular cluster follows the galaxy mass −metallicity relation) suggest that even the oldest, most metal-poor globular clusters form at $z < 5.9$, i.e., after the reionization of the early universe.

The interacting galaxies in the SMACS0723 galaxy cluster environment may be the place to look for evidence of the formation of compact star clusters at $z = 0.39$—approximately 4.3 Gyr before the observation of the Milky Way or a local globular cluster. The galaxies are clearly interacting as shown by the evident diffuse intracluster light (e.g., Pascale et al. 2022), suggestive of stars being stripped from the galaxies. The new JWST/NIRCam observations at 1–5 μm show a considerable amount of relatively blue and faint (>28 AB mag) point sources around the cluster members (see also Lee et al. 2022). As shown in Section 3.5, this number of faint point sources cannot be explained by Milky Way stars, nor globular clusters in the Milky Way, which, at sizes of ∼10 pc, would be resolved and significantly brighter. These objects are good candidates for globular clusters and their study may inform us about the formation of globular clusters at higher redshifts.

The large angular coverage of the two NIRCam fields of view (FoVs), being offset from each other by ∼1 Mpc at the cluster's redshift, allow also a spatial study of globular clusters around the brightest cluster galaxy (BCG). If recently formed star clusters are stripped from their host galaxies due to the interactions in the galaxy cluster, we would expect these to be relatively young and metal abundant compared to those originating from an early formation scenario. Furthermore, the size and masses of these compact star clusters may differentiate them from stripped cores of dwarf galaxies (e.g., Ideta & Makino 2004).

This Letter is organized as follows: In Section 2, we detail the data used in this work, the selection of the compact star clusters, and various measurements. In Section 3, we present the results from our analysis. We conclude in Section 4. Throughout this work, we assume a ΛCDM cosmology with $H_0 = 70\,\mathrm{km\,s^{-1}\,Mpc^{-1}}$, $\Omega_\Lambda = 0.7$, and $\Omega_\mathrm{m} = 0.3$. All magnitudes are given in the AB system (Oke 1974), and stellar masses and star formation rates (SFRs) are normalized to a Chabrier (2003) initial mass function (IMF) unless noted differently.

2. Data and Measurements

2.1. Data

In this work, we focus on compact stellar clusters in the galaxy cluster environment SMACS J0723.3–7327 at $z = 0.39$ ($07^\mathrm{h}23^\mathrm{m}13^\mathrm{s}.3$, $-73^\mathrm{d}27^\mathrm{m}25^\mathrm{s}$). SMACS0723 was initially discovered as part of the southern extension to the ROSAT All-Sky Survey (Voges et al. 1999) based Massive Cluster Survey (MACS; Ebeling et al. 2001) and also detected by Planck (Planck Collaboration et al. 2011) through the Sunyaev–Zel'dovich effect. It was then subsequently studied by the Reionization Lensing Cluster Survey (RELICS) using the Hubble Space Telescope (HST; Coe et al. 2019). A new study using JWST by Mahler et al. (2022) places the total mass of the cluster at $M_{<400\,\mathrm{kpc}} = 3 \times 10^{14}\,M_\odot$ (compared to the measurement by Planck of $M_{500} = 8 \times 10^{14}\,M_\odot$). The BCG has a stellar mass of $\sim 2 \times 10^{11}\,M_\odot$ (close to the "knee" of the galaxy stellar mass function; e.g., Davidzon et al. 2017) and resembles a relatively featureless elliptical galaxy with little to no ongoing star formation. Here, we use new JWST observations of the cluster (ERO program ID 2736; Pontoppidan et al. 2022) taken with the Near Infrared Camera (NIRCam; Rieke et al. 2005) broadband filters F090W (0.90 μm), F150W (1.50 μm), F200W (1.99 μm), F277W (2.76 μm), F356W (3.57 μm), and F444W (4.41 μm). These filters correspond to wavelengths in the cluster's rest frame of 0.65, 1.08, 1.43, 1.98, 2.57, and 3.17 μm, respectively. NIRCam consists of two modules, each observing a $2'.2 \times 2'.2$ FoV, one centered on the cluster's BCG and the other one centered $\sim 3'$ (∼1 Mpc at the cluster's redshift) to the southwest. The data were downloaded from the Mikulski Archive of Space Telescopes (MAST)[4] and subsequently reduced with the JWST data reduction pipeline. The reduced image data was then combined using the grism redshift and line analysis software for space-based spectroscopy (GRIZLI; Brammer & Matharu 2021) package to a final pixel scale of $0''.02$ px for F090W, F150W, and F200W and $0''.04$ px for F277W, F356W, and F444W, respectively (Brammer 2022). Note that the recent `jwst_0942.pmap` photometric calibration reference file was used with modifications as of 2022 September 5 as described in the GRIZLI GitHub repository.[5] The details of the data reduction will be presented in detail in an upcoming paper (G. Brammer et al. 2022, in preparation). The field was also imaged by JWST/MIRI at mid-infrared wavelengths. However, the MIRI data are too shallow for this study and are therefore not being used. Figure 1 shows an overview of the data used.

2.2. Source Selection

In this work, we study the faintest, compact stellar clusters in the SMACS0723 field, such as potential globular clusters around the cluster host galaxies. These sources are selected manually mainly on the F200W image; however, we require them also to be detected in at least two other bands in order to reject potential spurious sources. In addition, the sources are selected to be unresolved point sources as well as faint (to exclude Milky Way stars; see Section 3.5). For example, a good upper limit in size of globular cluster is ∼10 pc (e.g., Larsen et al. 2001), which, at $z = 0.39$, corresponds to an angular size of ∼1.4 mas (note that there are some larger globular clusters, for example NGC 2419 in the Milky Way and Lindsay 1 in the Small Magellanic Cloud). This is significantly smaller than the point-spread function (PSF) size (between 20 and 120 mas at 1–5 μm), thus motivating the point-source assumption. Milky Way stars are the most likely contaminants in this selection, as discussed in Section 3.5. We tried an automated selection of globular clusters; however, we found that this approach results in a severely incomplete selection due to blending with the BCG and other cluster galaxies, as well as the variation of the intracluster and scattered light across the field. In total, we identified 178 compact star clusters in the full FoV of NIRCam around the cluster host galaxies (see Figure 1), which we characterize and

---

[4] https://mast.stsci.edu/

[5] https://github.com/gbrammer/grizli/pull/107

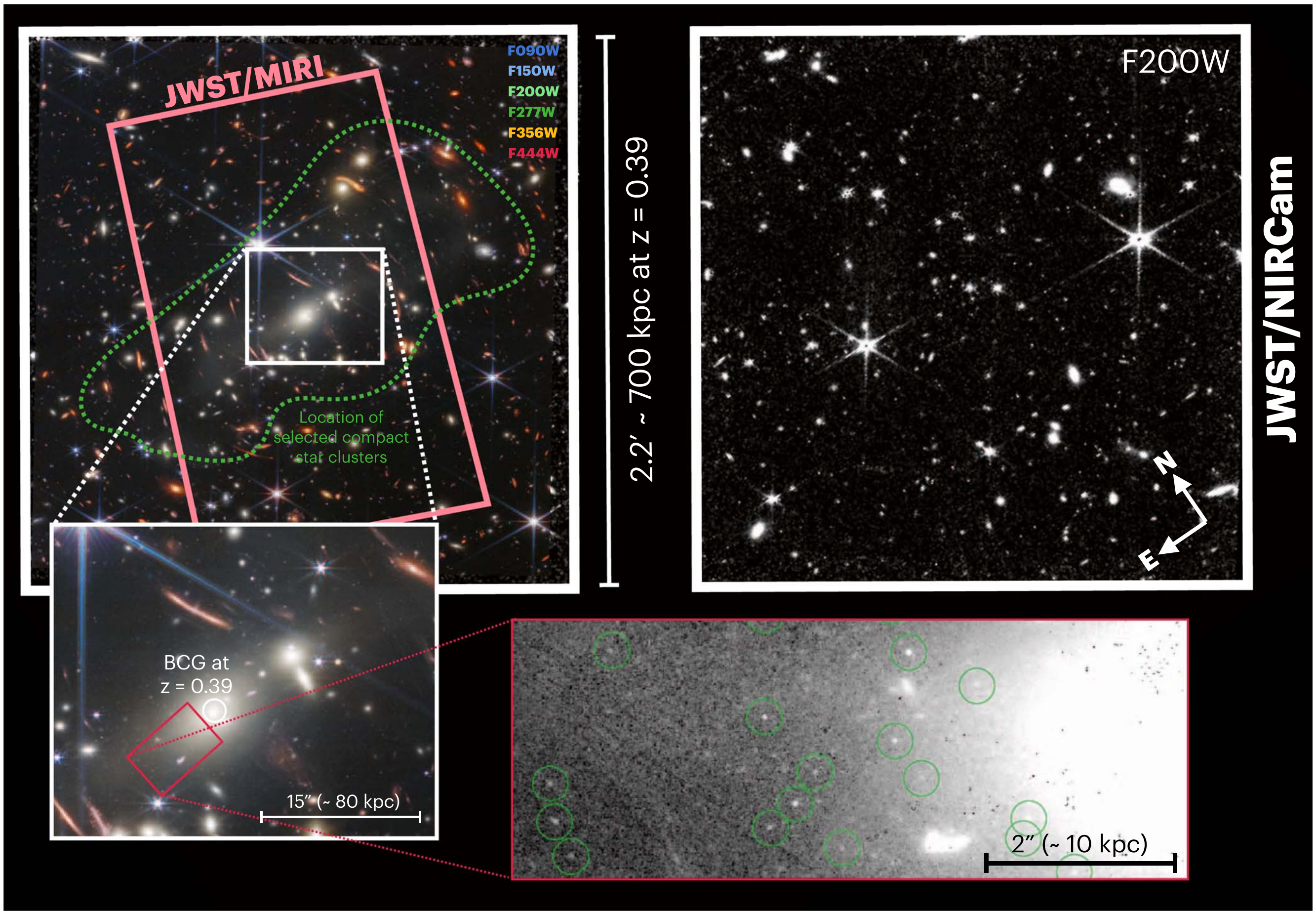

Figure 1. Overview of data used in this study. The large white squares are the 2.′2 × 2.′2 FoVs of the two NIRCam modules. The left one is centered on the cluster BCG (color composite of all six observed NIRCam filters) and the right one (F200W shown only) is offset by approximately 3′ (or ∼1 Mpc at cluster redshift). The location of the selected compact star clusters studied in this work is marked with the green dashed contour. The JWST/MIRI coverage (red) is indicated for completeness, although MIRI data are not used in this study. The red inset shows an example selection of globular cluster (green circles) close to the BCG.

study in the following. The coordinates and NIRCam fluxes of the extracted star clusters are listed in Table 1. We note that our selection is not complete, but serves as a starting point to understand the properties and origin of these faint sources. We refer to the work by Lee et al. (2022) for a detailed study of the distribution and number density of these star clusters in the ICM of SMACS0723. If these sources are globular clusters, we would expect to only see the tip of the iceberg (i.e., the brightest ones) even at the unprecedented depths of these observations, assuming the commonly used Gaussian globular cluster luminosity function (e.g., Alamo-Martínez et al. 2013).

2.3. *Measurement of the PSF*

To measure the photometry of unresolved point sources, a robust determination of the PSF is crucial. Here, we measure the PSF in all six NIRCam filters by stacking stars on the full FoV of the available observations. For the selection of stars, we use an identical approach as in Faisst et al. (2022). Summarizing, the stars are selected based on the R_e versus magnitude diagram (produced by the `flux_radius` and `flux_auto` quantities derived by SExtractor, Bertin & Arnouts 1996, run the NIRCam images). We note that, based on the upturn in size measurements on that diagram, point sources at ∼25 mag already start to enter the nonlinear regime toward saturation at the depth of these NIRCam observations. We therefore require stars between 25 and 27 mag, to avoid the aforementioned saturation effect, as well as to exclude potential faint, spurious sources. In addition, a half-light radius of less than 3 pixels is required to select unresolved sources. For each of the 58 stars, we create a 2″ × 2″ cutout and subsequently center the stars before stacking them to obtain the final PSF. The final PSF for each filter (normalized and of the same pixel scale as the images; see Section 2.1) are available for download.[6]

The relatively low number density of stars does not allow us to quantify variations of the PSF. However, the recent study by Nardiello et al. (2022) measured PSF variations across the NIRCam FoV based on stars in the globular cluster M92, finding variations in the FWHM of up to 15%–20%. Such variations have a negligible effect on the measured photometry in our case, but we will include this effect later when we constrain the sizes of our compact star clusters.

2.4. *Measurement of Photometry*

The photometry of the selected globular cluster is measured using the software Tractor[7] (Lang et al. 2016a, 2016b; J. Weaver et al. 2022, in preparation), which performs a prior-

---

[6] https://github.com/afaisst/JWST_SMACS_PSFs

[7] http://thetractor.org/

Table 1
Coordinates, NIRCam Fluxes, and Stellar Masses for All Extracted Compact Star Clusters

ID	R.A. (J2000)	Decl. (J2000)	F090W (nJy)	F150W (nJy)	F200W (nJy)	F277W (nJy)	F356W (nJy)	F444W (nJy)	$\log(M/M_\odot)$
SC_000	110.83478	−73.45518	9.4 ± 1.2	22.7 ± 0.3	20.3 ± 0.3	21.6 ± 1.2	12.0 ± 1.1	11.2 ± 1.5	6.73 ± 0.05
SC_001	110.83487	−73.45463	20.5 ± 1.2	29.2 ± 0.5	33.8 ± 0.7	30.7 ± 0.6	15.4 ± 1.1	13.4 ± 1.5	7.02 ± 0.02
SC_002	110.83238	−73.45431	34.9 ± 1.2	57.5 ± 0.8	70.3 ± 0.7	67.7 ± 0.5	39.6 ± 0.5	33.7 ± 0.5	7.25 ± 0.02
SC_003	110.83262	−73.45475	29.8 ± 1.2	29.8 ± 0.7	33.3 ± 0.7	31.5 ± 1.1	17.3 ± 0.7	12.8 ± 1.5	6.52 ± 0.02
SC_004	110.83263	−73.45367	12.8 ± 1.2	20.8 ± 0.7	14.7 ± 0.5	10.6 ± 1.2	11.1 ± 0.7	4.5 ± 1.5	6.68 ± 0.04
SC_005	110.82962	−73.45353	16.4 ± 1.2	16.7 ± 0.5	19.2 ± 0.5	12.2 ± 0.8	9.4 ± 0.6	7.6 ± 1.5	6.59 ± 0.03
SC_006	110.83044	−73.45322	15.5 ± 1.2	20.0 ± 0.5	22.5 ± 0.7	16.3 ± 1.2	11.1 ± 0.7	6.4 ± 1.5	6.94 ± 0.04
SC_007	110.82800	−73.45331	3.2 ± 1.2	12.2 ± 0.7	14.0 ± 0.7	18.9 ± 0.5	16.6 ± 1.1	15.7 ± 1.5	5.75 ± 0.14
SC_008	110.82647	−73.45389	23.8 ± 1.2	20.6 ± 0.5	19.7 ± 0.6	25.2 ± 0.8	9.5 ± 1.1	8.6 ± 1.5	6.27 ± 0.02
SC_009	110.82579	−73.45360	21.7 ± 1.2	26.3 ± 0.5	27.0 ± 0.4	24.6 ± 0.7	15.0 ± 1.1	11.7 ± 0.7	6.42 ± 0.02
SC_010	110.82474	−73.45357	5.3 ± 1.2	14.9 ± 0.4	18.9 ± 0.4	13.0 ± 1.2	11.4 ± 1.1	7.8 ± 1.5	6.62 ± 0.09
SC_011	110.82139	−73.45397	17.0 ± 1.2	18.6 ± 0.6	18.0 ± 0.3	14.9 ± 0.5	9.6 ± 0.7	5.9 ± 1.5	6.46 ± 0.03
SC_012	110.82147	−73.45443	6.3 ± 1.2	16.8 ± 0.8	14.9 ± 0.7	12.8 ± 1.2	11.5 ± 1.1	1.8 ± 1.5	6.65 ± 0.10
SC_013	110.82276	−73.45429	7.5 ± 1.2	16.6 ± 0.7	20.8 ± 0.4	15.2 ± 1.2	2.0 ± 1.1	5.4 ± 1.5	6.55 ± 0.07
SC_014	110.82239	−73.45520	14.7 ± 1.2	17.8 ± 0.8	22.2 ± 0.6	20.7 ± 1.2	12.0 ± 1.1	13.3 ± 1.5	6.50 ± 0.04
SC_015	110.82412	−73.45540	26.1 ± 1.2	42.1 ± 0.2	42.7 ± 0.3	47.2 ± 1.2	27.2 ± 1.0	21.7 ± 1.5	6.36 ± 0.02
SC_016	110.82460	−73.45579	15.2 ± 1.2	16.6 ± 0.5	18.5 ± 0.5	19.5 ± 1.1	7.3 ± 1.1	7.4 ± 1.1	6.13 ± 0.03
SC_017	110.82441	−73.45585	8.1 ± 1.2	14.6 ± 0.6	13.0 ± 0.5	16.9 ± 0.5	15.3 ± 0.9	13.5 ± 1.5	5.92 ± 0.06
SC_018	110.82575	−73.45549	20.8 ± 1.2	28.0 ± 0.6	21.5 ± 0.5	21.9 ± 1.2	16.8 ± 1.1	16.7 ± 1.5	6.16 ± 0.02
SC_019	110.82953	−73.45540	18.3 ± 1.2	21.3 ± 0.8	28.3 ± 0.2	33.8 ± 1.2	20.3 ± 1.1	24.1 ± 1.5	6.52 ± 0.02
SC_020	110.83033	−73.45513	26.0 ± 1.2	34.4 ± 0.4	38.6 ± 0.4	42.2 ± 1.2	26.4 ± 1.1	13.8 ± 1.5	6.43 ± 0.02
SC_021	110.83040	−73.45523	12.0 ± 1.2	21.5 ± 0.7	27.5 ± 0.6	39.3 ± 1.2	29.3 ± 1.1	30.0 ± 1.5	6.34 ± 0.04
SC_022	110.83355	−73.45528	11.5 ± 1.2	12.9 ± 0.5	13.0 ± 0.6	12.9 ± 1.0	5.3 ± 1.1	6.3 ± 1.5	5.95 ± 0.05
SC_023	110.83300	−73.45532	6.8 ± 1.2	15.5 ± 0.5	14.4 ± 0.5	13.7 ± 1.0	7.1 ± 0.7	6.2 ± 1.5	6.63 ± 0.08
SC_024	110.83395	−73.45505	15.7 ± 0.1	15.8 ± 0.6	11.1 ± 0.6	10.1 ± 1.2	3.8 ± 1.1	1.2 ± 1.5	6.22 ± 0.00
SC_025	110.83219	−73.45462	19.3 ± 1.2	22.8 ± 0.6	24.3 ± 0.7	20.5 ± 0.5	17.1 ± 1.0	12.7 ± 1.5	6.37 ± 0.03
SC_026	110.83015	−73.45389	19.9 ± 0.0	30.4 ± 0.8	34.9 ± 0.5	36.0 ± 0.9	18.9 ± 0.7	18.3 ± 1.5	6.18 ± 0.00
SC_027	110.82938	−73.45402	12.7 ± 1.2	17.0 ± 0.8	21.8 ± 0.5	17.4 ± 1.2	12.8 ± 1.1	9.3 ± 1.5	6.49 ± 0.04
SC_028	110.83031	−73.45406	18.4 ± 1.2	14.4 ± 0.7	14.7 ± 0.6	19.7 ± 1.2	9.2 ± 1.1	10.7 ± 1.5	6.11 ± 0.03
SC_029	110.83097	−73.45398	4.4 ± 1.2	13.7 ± 0.8	12.0 ± 0.5	9.8 ± 0.4	2.3 ± 1.1	2.5 ± 1.5	6.17 ± 0.12
SC_030	110.83071	−73.45574	46.2 ± 1.2	55.4 ± 0.4	59.1 ± 0.7	52.6 ± 1.2	29.8 ± 0.5	20.5 ± 1.5	7.08 ± 0.01
SC_031	110.83011	−73.45603	10.3 ± 1.2	21.3 ± 0.8	18.8 ± 0.6	15.2 ± 0.3	9.5 ± 1.1	4.6 ± 1.5	6.76 ± 0.04
SC_032	110.83222	−73.45585	10.8 ± 1.2	13.2 ± 0.4	14.6 ± 0.5	13.4 ± 1.2	7.1 ± 0.1	2.9 ± 1.5	6.76 ± 0.04
SC_033	110.82036	−73.45593	5.2 ± 1.2	12.7 ± 0.8	13.1 ± 0.5	15.8 ± 0.6	7.3 ± 1.0	6.0 ± 1.5	6.53 ± 0.09
SC_034	110.82258	−73.45596	10.0 ± 1.2	12.7 ± 0.3	12.6 ± 0.4	8.3 ± 1.2	3.7 ± 1.1	3.3 ± 1.5	6.68 ± 0.05
SC_035	110.80869	−73.45551	15.6 ± 1.2	18.8 ± 0.5	20.8 ± 0.5	19.6 ± 0.6	10.4 ± 1.1	6.6 ± 1.5	6.37 ± 0.04
SC_036	110.81668	−73.45396	15.0 ± 1.2	10.1 ± 0.6	13.3 ± 0.5	16.7 ± 1.2	7.7 ± 1.1	8.0 ± 1.5	6.12 ± 0.04
SC_037	110.81672	−73.45406	3.9 ± 1.2	21.2 ± 0.8	19.9 ± 0.4	16.8 ± 0.9	7.1 ± 0.6	3.5 ± 1.5	6.45 ± 0.14
SC_038	110.81860	−73.45359	6.8 ± 1.2	20.8 ± 0.7	23.1 ± 0.6	24.1 ± 1.2	14.1 ± 1.1	7.6 ± 1.5	6.89 ± 0.07
SC_039	110.82047	−73.45328	31.2 ± 1.2	32.3 ± 0.4	32.5 ± 0.4	31.2 ± 0.5	20.6 ± 0.5	8.4 ± 1.5	6.38 ± 0.01
SC_040	110.82181	−73.45330	12.8 ± 1.2	19.8 ± 0.1	15.7 ± 0.2	16.9 ± 1.2	15.1 ± 1.1	15.6 ± 1.5	6.12 ± 0.04
SC_041	110.82086	−73.45378	2.8 ± 1.2	11.5 ± 0.7	11.6 ± 0.4	8.6 ± 1.2	7.5 ± 0.7	2.9 ± 1.5	6.32 ± 0.18
SC_042	110.82852	−73.45620	12.0 ± 0.1	17.6 ± 0.4	17.1 ± 0.6	16.0 ± 0.4	8.8 ± 1.1	5.9 ± 1.5	6.37 ± 0.00
SC_043	110.82804	−73.45646	17.9 ± 1.2	20.7 ± 0.8	15.5 ± 0.3	15.2 ± 1.2	8.4 ± 1.1	6.9 ± 1.5	6.26 ± 0.03
SC_044	110.82936	−73.45614	18.6 ± 1.2	17.1 ± 0.5	18.0 ± 0.5	20.0 ± 1.2	16.6 ± 1.1	21.3 ± 1.5	6.28 ± 0.03
SC_045	110.82436	−73.45603	8.0 ± 1.2	14.9 ± 0.7	16.0 ± 0.6	13.3 ± 0.8	6.9 ± 1.1	1.9 ± 1.5	6.39 ± 0.06
SC_046	110.82245	−73.45393	11.0 ± 1.2	13.9 ± 0.3	11.9 ± 0.5	11.0 ± 0.3	4.6 ± 0.7	4.4 ± 1.5	6.59 ± 0.04
SC_047	110.82245	−73.45386	9.5 ± 1.2	14.6 ± 0.7	14.3 ± 0.6	14.5 ± 0.6	18.8 ± 0.4	10.9 ± 1.5	5.99 ± 0.06
SC_048	110.82226	−73.45405	6.0 ± 1.2	7.1 ± 0.6	8.2 ± 0.5	7.4 ± 1.2	8.3 ± 1.1	1.9 ± 1.5	5.95 ± 0.09
SC_049	110.81272	−73.45459	19.8 ± 1.2	25.4 ± 0.8	25.6 ± 0.6	21.9 ± 1.2	12.9 ± 1.1	9.5 ± 1.5	7.05 ± 0.02
SC_050	110.82056	−73.45527	10.7 ± 1.2	20.9 ± 0.8	20.4 ± 0.6	24.2 ± 1.2	10.7 ± 0.7	12.8 ± 1.5	6.74 ± 0.04
SC_051	110.83121	−73.45448	10.5 ± 1.2	18.1 ± 0.8	18.0 ± 0.6	17.6 ± 1.2	10.5 ± 1.1	9.6 ± 1.5	6.80 ± 0.05
SC_052	110.83858	−73.45495	12.0 ± 1.2	19.7 ± 0.8	18.9 ± 0.4	17.0 ± 1.2	10.8 ± 1.1	6.6 ± 1.5	6.36 ± 0.05
SC_053	110.83849	−73.45514	19.3 ± 1.2	24.8 ± 0.6	22.9 ± 0.5	22.8 ± 0.7	13.3 ± 0.7	7.7 ± 1.5	6.17 ± 0.02
SC_054	110.83820	−73.45532	9.5 ± 1.2	8.4 ± 0.6	10.7 ± 0.7	11.2 ± 1.2	5.0 ± 1.1	4.8 ± 1.5	5.93 ± 0.06
SC_055	110.83400	−73.45490	6.1 ± 1.2	9.3 ± 0.8	15.3 ± 0.6	15.0 ± 1.1	6.4 ± 1.1	7.5 ± 1.5	6.75 ± 0.10
SC_056	110.83486	−73.45413	7.2 ± 1.2	11.4 ± 0.6	12.0 ± 0.3	9.5 ± 1.2	7.8 ± 1.1	8.4 ± 1.5	6.63 ± 0.07
SC_057	110.82368	−73.45312	7.7 ± 1.2	11.5 ± 0.5	16.3 ± 0.2	13.4 ± 0.6	8.0 ± 1.1	2.2 ± 1.5	6.78 ± 0.07
SC_058	110.82875	−73.45347	5.8 ± 1.2	8.2 ± 0.6	10.7 ± 0.5	8.6 ± 1.2	5.3 ± 1.1	4.1 ± 1.5	6.20 ± 0.07
SC_059	110.84541	−73.45423	9.5 ± 1.2	17.9 ± 0.5	15.5 ± 0.7	11.1 ± 1.2	5.6 ± 1.1	7.5 ± 0.3	6.72 ± 0.06
SC_060	110.84582	−73.45393	6.3 ± 1.2	12.8 ± 0.6	11.3 ± 0.7	10.0 ± 1.2	7.9 ± 1.0	6.0 ± 0.5	6.58 ± 0.08
SC_061	110.84403	−73.45389	3.9 ± 1.1	10.4 ± 0.8	11.2 ± 0.2	11.9 ± 1.2	6.3 ± 1.1	4.7 ± 1.5	6.68 ± 0.14
SC_062	110.84351	−73.45305	9.3 ± 1.2	14.2 ± 0.8	12.2 ± 0.7	11.7 ± 1.2	6.9 ± 1.1	3.0 ± 1.5	6.72 ± 0.06

Table 1
(Continued)

ID	R.A. (J2000)	Decl. (J2000)	F090W (nJy)	F150W (nJy)	F200W (nJy)	F277W (nJy)	F356W (nJy)	F444W (nJy)	$\log(M/M_\odot)$
SC_063	110.84426	−73.45268	7.1 ± 0.1	19.4 ± 0.5	19.6 ± 0.5	19.7 ± 1.2	9.7 ± 0.8	6.6 ± 1.5	6.56 ± 0.01
SC_064	110.84474	−73.45277	10.8 ± 1.2	18.6 ± 0.8	19.3 ± 0.6	21.3 ± 1.2	12.0 ± 1.1	8.3 ± 1.5	6.83 ± 0.05
SC_065	110.84351	−73.45347	2.0 ± 1.2	13.4 ± 0.7	14.9 ± 0.7	11.8 ± 1.2	6.6 ± 0.0	3.1 ± 1.5	5.23 ± 0.22
SC_066	110.83753	−73.45430	10.7 ± 1.2	16.5 ± 0.5	12.7 ± 0.7	18.2 ± 1.2	12.1 ± 0.5	7.0 ± 1.5	6.04 ± 0.05
SC_067	110.82613	−73.45409	4.1 ± 1.2	24.4 ± 0.7	21.5 ± 0.6	28.9 ± 1.2	17.8 ± 1.1	28.6 ± 1.5	6.69 ± 0.13
SC_068	110.83132	−73.45512	4.6 ± 1.2	6.0 ± 0.8	10.7 ± 0.6	5.3 ± 1.1	1.9 ± 1.1	0.8 ± 1.5	6.06 ± 0.11
SC_069	110.82314	−73.45583	42.1 ± 1.2	53.0 ± 0.0	37.3 ± 0.1	32.8 ± 1.1	35.2 ± 1.1	29.7 ± 1.5	6.50 ± 0.02
SC_070	110.82385	−73.45596	17.6 ± 1.2	26.8 ± 0.8	29.5 ± 0.7	28.9 ± 1.2	18.3 ± 1.0	13.9 ± 1.5	6.57 ± 0.03
SC_071	110.83472	−73.45482	6.5 ± 1.2	12.4 ± 0.7	11.3 ± 0.4	9.5 ± 1.2	5.9 ± 1.1	8.6 ± 1.5	6.57 ± 0.08
SC_072	110.84418	−73.45358	7.7 ± 1.2	7.2 ± 0.2	5.2 ± 0.7	7.2 ± 1.2	4.4 ± 1.1	5.7 ± 1.5	5.74 ± 0.05
SC_073	110.84534	−73.45344	8.4 ± 1.2	13.2 ± 0.7	15.0 ± 0.7	13.5 ± 1.0	6.5 ± 1.1	5.3 ± 1.5	6.59 ± 0.06
SC_074	110.80991	−73.45428	7.1 ± 1.2	5.8 ± 0.8	7.3 ± 0.6	6.1 ± 1.2	5.8 ± 1.1	-0.1 ± 1.5	6.47 ± 0.07
SC_075	110.81175	−73.45398	4.1 ± 1.2	11.9 ± 0.4	13.9 ± 0.7	10.8 ± 1.2	7.9 ± 1.0	3.8 ± 1.5	6.48 ± 0.15
SC_076	110.81713	−73.45409	12.9 ± 1.2	22.3 ± 0.0	17.0 ± 0.6	17.3 ± 1.2	12.1 ± 0.7	6.3 ± 1.5	5.99 ± 0.04
SC_077	110.82002	−73.45379	20.2 ± 1.2	21.5 ± 0.5	20.4 ± 0.7	-0.7 ± 1.2	-1.2 ± 1.1	-2.9 ± 1.5	6.92 ± 0.03
SC_078	110.83525	−73.45489	4.9 ± 1.2	8.4 ± 0.6	12.0 ± 0.7	12.5 ± 1.2	6.9 ± 1.1	4.3 ± 1.4	6.24 ± 0.11
SC_079	110.83585	−73.45481	6.6 ± 1.2	11.6 ± 0.8	11.6 ± 0.7	11.3 ± 1.2	6.2 ± 0.8	1.7 ± 1.5	6.30 ± 0.09
SC_080	110.84533	−73.45445	7.7 ± 1.2	14.5 ± 0.7	14.1 ± 0.5	14.0 ± 1.1	7.5 ± 1.1	3.9 ± 1.5	6.75 ± 0.06
SC_081	110.84509	−73.45449	4.9 ± 1.2	10.0 ± 0.7	9.8 ± 0.4	7.9 ± 1.2	4.6 ± 0.6	-2.5 ± 1.5	6.28 ± 0.11
SC_082	110.82796	−73.45581	4.7 ± 1.2	8.8 ± 0.8	12.6 ± 0.6	8.9 ± 1.2	8.7 ± 1.1	4.8 ± 1.5	6.55 ± 0.12
SC_083	110.82717	−73.45708	7.1 ± 1.2	18.8 ± 0.6	20.3 ± 0.5	19.4 ± 0.7	11.0 ± 1.0	8.0 ± 1.5	6.63 ± 0.07
SC_084	110.78770	−73.45499	6.6 ± 1.2	10.7 ± 0.6	9.7 ± 0.6	10.5 ± 1.2	3.8 ± 1.1	6.5 ± 0.5	6.15 ± 0.07
SC_085	110.81329	−73.45452	23.5 ± 1.2	13.6 ± 0.8	14.3 ± 0.5	2.1 ± 1.2	1.8 ± 1.1	-0.4 ± 1.5	6.98 ± 0.02
SC_086	110.82160	−73.45648	7.5 ± 1.2	8.3 ± 0.8	13.7 ± 0.7	10.9 ± 0.8	5.8 ± 1.0	7.8 ± 1.5	6.37 ± 0.07
SC_087	110.81876	−73.45635	10.8 ± 0.1	11.7 ± 0.8	15.3 ± 0.7	10.6 ± 1.2	5.0 ± 1.0	5.3 ± 1.5	6.75 ± 0.00
SC_088	110.81799	−73.45675	2.8 ± 1.2	8.5 ± 0.8	7.8 ± 0.5	9.5 ± 0.4	5.3 ± 1.1	2.3 ± 1.5	5.73 ± 0.19
SC_089	110.81732	−73.45681	11.4 ± 1.2	12.8 ± 0.7	13.3 ± 0.4	11.0 ± 0.7	4.5 ± 1.1	4.0 ± 1.5	6.45 ± 0.04
SC_090	110.81038	−73.45548	14.1 ± 1.2	17.6 ± 0.7	18.7 ± 0.7	21.8 ± 1.2	12.9 ± 1.1	12.1 ± 1.5	6.16 ± 0.04
SC_091	110.78922	−73.45409	14.0 ± 0.7	8.6 ± 0.6	9.6 ± 0.4	10.2 ± 0.9	4.7 ± 1.1	3.1 ± 1.5	6.02 ± 0.02
SC_092	110.78970	−73.45433	7.7 ± 1.2	10.8 ± 0.5	11.2 ± 0.4	8.8 ± 1.2	4.7 ± 0.7	5.5 ± 1.5	6.64 ± 0.07
SC_093	110.79125	−73.45385	9.8 ± 1.2	10.2 ± 0.5	10.7 ± 0.5	9.8 ± 1.2	3.5 ± 1.1	2.4 ± 1.5	6.33 ± 0.05
SC_094	110.78340	−73.45303	6.7 ± 0.1	8.2 ± 0.5	9.5 ± 0.4	7.4 ± 1.2	2.8 ± 1.1	2.2 ± 1.5	6.57 ± 0.01
SC_095	110.78423	−73.45257	1.9 ± 1.2	6.7 ± 0.4	7.7 ± 0.4	6.8 ± 1.2	2.8 ± 1.1	1.2 ± 1.5	6.41 ± 0.24
SC_096	110.78713	−73.45280	22.1 ± 1.2	22.9 ± 0.6	23.7 ± 0.7	21.4 ± 1.2	12.1 ± 0.8	9.5 ± 1.5	6.64 ± 0.03
SC_097	110.78789	−73.45194	13.2 ± 1.2	17.7 ± 0.4	18.5 ± 0.5	14.6 ± 1.2	9.5 ± 1.1	5.8 ± 1.5	6.86 ± 0.03
SC_098	110.78635	−73.45047	7.2 ± 1.2	14.7 ± 0.6	14.0 ± 0.4	18.4 ± 1.2	10.8 ± 0.6	9.2 ± 1.5	5.88 ± 0.08
SC_099	110.78172	−73.45070	10.3 ± 1.2	9.8 ± 0.8	10.8 ± 0.6	9.1 ± 0.6	4.5 ± 1.1	1.8 ± 1.5	6.35 ± 0.04
SC_100	110.79601	−73.44790	6.0 ± 1.2	16.9 ± 0.7	19.2 ± 0.5	18.7 ± 1.2	9.8 ± 0.6	6.0 ± 1.5	6.83 ± 0.08
SC_101	110.79508	−73.44825	14.7 ± 1.2	13.2 ± 0.7	14.7 ± 0.7	13.0 ± 1.2	6.2 ± 0.8	10.0 ± 1.5	6.30 ± 0.04
SC_102	110.79584	−73.44829	9.4 ± 1.2	16.7 ± 0.7	15.7 ± 0.4	14.3 ± 1.2	8.9 ± 1.1	7.0 ± 1.5	6.32 ± 0.06
SC_103	110.80174	−73.44977	13.2 ± 1.2	17.9 ± 0.6	17.8 ± 0.5	19.1 ± 0.7	9.5 ± 1.1	8.6 ± 1.5	6.07 ± 0.05
SC_104	110.80198	−73.44992	9.3 ± 1.2	13.8 ± 0.4	16.7 ± 0.1	14.3 ± 1.1	8.0 ± 1.0	5.7 ± 1.5	6.75 ± 0.06
SC_105	110.80116	−73.44958	9.9 ± 1.2	16.3 ± 0.7	16.0 ± 0.5	18.8 ± 0.6	13.8 ± 1.1	14.2 ± 1.5	6.00 ± 0.04
SC_106	110.80534	−73.44852	8.6 ± 1.2	11.5 ± 0.7	16.0 ± 0.5	9.4 ± 0.5	8.0 ± 0.5	6.0 ± 1.5	6.29 ± 0.05
SC_107	110.80524	−73.44870	8.0 ± 1.2	10.6 ± 0.3	8.2 ± 0.7	11.9 ± 1.2	5.5 ± 0.9	2.2 ± 1.5	5.75 ± 0.06
SC_108	110.78716	−73.45552	8.9 ± 1.2	14.5 ± 0.5	15.0 ± 0.5	15.0 ± 1.2	9.2 ± 1.1	7.6 ± 1.5	6.28 ± 0.06
SC_109	110.78741	−73.45586	9.9 ± 1.2	11.8 ± 0.7	15.5 ± 0.6	12.2 ± 1.2	6.4 ± 0.5	4.2 ± 0.4	6.72 ± 0.06
SC_110	110.78030	−73.45425	7.6 ± 1.2	13.3 ± 0.5	14.7 ± 0.6	12.7 ± 0.4	6.1 ± 0.7	3.1 ± 1.5	6.55 ± 0.07
SC_111	110.78126	−73.45340	5.6 ± 1.2	11.9 ± 0.4	15.3 ± 0.7	15.7 ± 0.4	9.0 ± 1.1	8.3 ± 1.5	6.76 ± 0.08
SC_112	110.78087	−73.45291	10.7 ± 1.2	17.9 ± 0.5	20.0 ± 0.5	20.6 ± 1.2	13.2 ± 0.9	8.3 ± 1.5	6.75 ± 0.04
SC_113	110.79191	−73.45265	9.3 ± 1.2	15.2 ± 0.7	14.4 ± 0.4	13.2 ± 1.2	8.5 ± 0.2	4.0 ± 1.5	6.27 ± 0.06
SC_114	110.79176	−73.45274	11.4 ± 1.2	13.2 ± 0.8	13.5 ± 0.6	10.8 ± 1.2	5.9 ± 1.1	5.0 ± 1.5	6.66 ± 0.04
SC_115	110.79931	−73.45132	7.9 ± 1.2	15.4 ± 0.7	13.7 ± 0.4	11.7 ± 0.8	6.4 ± 1.1	7.9 ± 1.5	6.65 ± 0.07
SC_116	110.79995	−73.45124	12.0 ± 1.2	9.8 ± 0.8	11.8 ± 0.6	10.0 ± 1.2	4.6 ± 0.3	6.4 ± 1.5	6.09 ± 0.04
SC_117	110.79854	−73.45139	4.4 ± 1.2	12.8 ± 0.5	10.2 ± 0.5	10.9 ± 1.2	5.4 ± 0.6	3.4 ± 1.5	6.41 ± 0.12
SC_118	110.79830	−73.45146	7.1 ± 1.2	8.5 ± 0.6	9.3 ± 0.4	10.9 ± 0.3	5.2 ± 0.6	0.2 ± 1.5	5.87 ± 0.07
SC_119	110.79798	−73.45131	7.7 ± 1.2	9.6 ± 0.5	11.5 ± 0.5	9.5 ± 1.2	5.3 ± 1.1	3.6 ± 1.5	6.25 ± 0.07
SC_120	110.79658	−73.45191	13.1 ± 1.2	15.0 ± 0.7	13.5 ± 0.6	11.4 ± 1.2	7.4 ± 0.7	2.6 ± 1.5	6.25 ± 0.04
SC_121	110.78631	−73.45810	23.0 ± 1.2	25.2 ± 0.8	24.1 ± 0.7	25.6 ± 1.2	19.6 ± 1.1	11.2 ± 1.5	6.26 ± 0.02
SC_122	110.78559	−73.45643	10.1 ± 1.2	14.8 ± 0.7	14.9 ± 0.3	13.9 ± 1.2	6.0 ± 1.1	5.0 ± 1.5	6.75 ± 0.05
SC_123	110.78135	−73.45553	8.2 ± 1.2	21.7 ± 0.7	19.7 ± 0.7	22.2 ± 1.2	14.3 ± 0.9	9.3 ± 1.5	6.86 ± 0.07
SC_124	110.67039	−73.48220	17.8 ± 1.2	14.8 ± 0.7	19.1 ± 0.7	26.5 ± 1.2	17.0 ± 1.1	14.8 ± 1.5	6.85 ± 0.03
SC_125	110.68257	−73.47759	15.3 ± 1.2	12.4 ± 0.6	16.0 ± 0.6	19.9 ± 1.2	8.7 ± 1.1	8.9 ± 1.5	6.79 ± 0.03

Table 1
(Continued)

ID	R.A. (J2000)	Decl. (J2000)	F090W (nJy)	F150W (nJy)	F200W (nJy)	F277W (nJy)	F356W (nJy)	F444W (nJy)	$\log(M/M_{\odot})$
SC_126	110.73865	−73.47510	5.6 ± 1.2	14.7 ± 0.6	14.0 ± 0.1	14.0 ± 1.2	29.0 ± 1.1	20.4 ± 1.5	6.35 ± 0.09
SC_127	110.70747	−73.49255	21.9 ± 1.2	32.1 ± 0.8	25.4 ± 0.5	34.1 ± 1.2	32.7 ± 1.1	33.2 ± 1.5	6.95 ± 0.02
SC_128	110.68775	−73.48465	15.1 ± 1.2	18.6 ± 0.8	13.4 ± 0.7	18.7 ± 0.5	21.6 ± 0.8	19.9 ± 1.5	6.79 ± 0.03
SC_129	110.69481	−73.48426	9.5 ± 1.2	13.6 ± 0.7	20.6 ± 0.7	37.8 ± 1.2	34.1 ± 1.0	35.6 ± 1.5	6.58 ± 0.06
SC_130	110.70230	−73.48263	8.9 ± 1.2	12.4 ± 0.8	12.8 ± 0.7	13.5 ± 0.8	14.8 ± 1.1	17.8 ± 1.5	6.56 ± 0.06
SC_131	110.69502	−73.48136	15.5 ± 1.2	18.3 ± 0.7	19.4 ± 0.7	29.6 ± 1.2	28.7 ± 1.1	24.5 ± 1.5	6.80 ± 0.03
SC_132	110.67261	−73.47396	15.6 ± 1.2	21.2 ± 0.8	19.9 ± 0.7	29.5 ± 1.2	21.2 ± 1.1	15.9 ± 1.5	6.81 ± 0.03
SC_133	110.85435	−73.45440	8.1 ± 1.2	10.3 ± 0.6	10.5 ± 0.7	7.0 ± 1.2	5.1 ± 1.1	3.9 ± 1.5	6.66 ± 0.06
SC_134	110.85244	−73.45419	3.8 ± 1.2	13.3 ± 0.6	13.6 ± 0.7	13.0 ± 1.2	8.3 ± 0.6	3.6 ± 1.5	6.61 ± 0.15
SC_135	110.85889	−73.45459	4.2 ± 1.2	12.8 ± 0.8	9.7 ± 0.6	6.7 ± 1.2	3.9 ± 0.8	0.6 ± 1.5	6.37 ± 0.10
SC_136	110.85791	−73.45462	6.6 ± 1.2	10.5 ± 0.7	10.9 ± 0.6	8.3 ± 0.7	5.7 ± 1.1	-1.6 ± 1.5	6.43 ± 0.08
SC_137	110.85896	−73.45420	6.3 ± 1.2	11.6 ± 0.6	12.0 ± 0.6	10.6 ± 0.9	4.7 ± 1.1	5.1 ± 1.5	6.46 ± 0.10
SC_138	110.86045	−73.45428	10.7 ± 1.2	12.3 ± 0.8	13.8 ± 0.7	12.1 ± 1.2	7.3 ± 1.1	6.5 ± 1.5	6.12 ± 0.06
SC_139	110.86098	−73.45427	6.2 ± 1.2	5.4 ± 0.6	6.0 ± 0.7	6.1 ± 1.2	4.0 ± 1.1	-0.0 ± 1.5	6.43 ± 0.07
SC_140	110.85891	−73.45394	10.7 ± 1.2	9.3 ± 0.7	10.6 ± 0.6	7.4 ± 0.6	4.3 ± 1.1	1.0 ± 1.5	6.15 ± 0.05
SC_141	110.82008	−73.46628	21.7 ± 1.2	27.3 ± 0.3	18.4 ± 0.7	15.3 ± 0.3	9.1 ± 0.8	5.6 ± 1.5	6.17 ± 0.03
SC_142	110.82292	−73.46619	0.9 ± 1.2	8.3 ± 0.8	9.5 ± 0.7	6.9 ± 1.2	5.4 ± 1.1	0.4 ± 1.5	6.29 ± 0.35
SC_143	110.79685	−73.45404	2.9 ± 1.2	7.2 ± 0.7	8.4 ± 0.4	7.2 ± 1.2	3.7 ± 0.3	3.5 ± 1.5	6.08 ± 0.22
SC_144	110.66959	−73.47230	4.1 ± 1.2	15.2 ± 0.5	14.1 ± 0.5	20.5 ± 0.5	61.5 ± 1.0	76.3 ± 1.5	6.21 ± 0.13
SC_145	110.81957	−73.45875	11.0 ± 1.2	13.2 ± 0.8	13.6 ± 0.4	9.7 ± 1.2	6.1 ± 0.6	5.3 ± 1.5	6.64 ± 0.05
SC_146	110.82110	−73.45871	5.1 ± 1.2	12.6 ± 0.5	12.4 ± 0.6	9.3 ± 1.2	4.7 ± 1.1	4.1 ± 1.5	6.37 ± 0.10
SC_147	110.82095	−73.45843	3.9 ± 1.2	8.1 ± 0.7	7.4 ± 0.7	6.5 ± 1.2	3.2 ± 1.1	2.5 ± 1.5	6.33 ± 0.14
SC_148	110.81494	−73.45791	9.8 ± 1.2	6.5 ± 0.7	8.5 ± 0.5	8.7 ± 0.5	6.0 ± 1.1	4.2 ± 1.5	5.93 ± 0.05
SC_149	110.81525	−73.45789	4.7 ± 1.2	9.2 ± 0.3	11.1 ± 0.5	11.4 ± 0.7	6.3 ± 1.1	5.7 ± 1.5	6.22 ± 0.09
SC_150	110.81370	−73.45776	10.4 ± 1.2	11.2 ± 0.6	11.8 ± 0.5	11.3 ± 0.7	6.9 ± 1.0	8.0 ± 1.5	5.96 ± 0.06
SC_151	110.81586	−73.45765	15.9 ± 1.2	25.2 ± 0.6	24.4 ± 0.6	22.4 ± 1.2	12.1 ± 0.6	9.4 ± 0.3	6.95 ± 0.03
SC_152	110.81782	−73.45708	21.2 ± 1.2	19.1 ± 0.7	20.1 ± 0.6	16.1 ± 1.2	9.0 ± 1.1	5.7 ± 1.5	6.46 ± 0.02
SC_153	110.82499	−73.45730	9.6 ± 1.2	27.0 ± 0.7	31.1 ± 0.5	26.5 ± 0.6	14.6 ± 1.1	10.0 ± 0.5	6.85 ± 0.05
SC_154	110.82503	−73.45740	6.7 ± 1.2	17.6 ± 0.3	16.3 ± 0.5	16.4 ± 1.2	15.2 ± 1.1	13.1 ± 1.5	6.78 ± 0.07
SC_155	110.82519	−73.45764	4.6 ± 1.2	9.7 ± 0.7	10.7 ± 0.7	8.3 ± 1.2	5.0 ± 0.7	5.9 ± 1.5	6.50 ± 0.12
SC_156	110.82888	−73.45774	10.3 ± 1.2	16.0 ± 0.7	17.5 ± 0.7	13.6 ± 1.2	8.8 ± 1.1	3.5 ± 1.5	6.36 ± 0.04
SC_157	110.88178	−73.45305	5.6 ± 1.2	13.1 ± 0.8	16.2 ± 0.5	12.4 ± 1.2	8.2 ± 1.1	4.5 ± 1.5	6.63 ± 0.09
SC_158	110.87357	−73.45284	9.0 ± 1.2	12.3 ± 0.8	10.6 ± 0.7	10.0 ± 1.2	4.2 ± 1.1	4.9 ± 1.5	6.52 ± 0.05
SC_159	110.87397	−73.45293	7.5 ± 0.1	7.0 ± 0.5	7.6 ± 0.7	9.3 ± 1.2	5.0 ± 1.0	1.6 ± 1.5	5.72 ± 0.01
SC_160	110.87266	−73.45103	9.4 ± 1.2	7.5 ± 0.6	7.1 ± 0.3	11.3 ± 1.2	5.6 ± 1.1	2.6 ± 1.5	5.82 ± 0.06
SC_161	110.87221	−73.45115	5.2 ± 1.2	5.5 ± 0.4	10.9 ± 0.5	9.1 ± 1.2	9.1 ± 1.1	8.8 ± 0.3	5.97 ± 0.09
SC_162	110.75752	−73.45268	7.9 ± 1.2	11.5 ± 0.8	12.1 ± 0.4	10.6 ± 1.2	5.3 ± 1.1	6.3 ± 1.5	6.26 ± 0.06
SC_163	110.75739	−73.45370	8.8 ± 1.2	14.7 ± 0.8	11.3 ± 0.5	6.9 ± 1.2	6.8 ± 1.1	5.5 ± 1.5	6.52 ± 0.05
SC_164	110.74766	−73.45285	18.4 ± 1.2	22.9 ± 0.2	20.9 ± 0.5	20.5 ± 1.2	10.0 ± 1.1	8.1 ± 1.5	6.83 ± 0.03
SC_165	110.74990	−73.44874	21.2 ± 1.2	29.8 ± 0.4	32.3 ± 0.5	27.7 ± 0.5	17.5 ± 0.6	14.4 ± 1.5	6.68 ± 0.02
SC_166	110.77654	−73.44677	13.1 ± 1.2	12.5 ± 0.7	10.7 ± 0.7	8.0 ± 0.5	5.9 ± 0.7	3.1 ± 1.5	6.12 ± 0.03
SC_167	110.77515	−73.44679	10.0 ± 1.2	10.5 ± 0.3	7.4 ± 0.3	16.1 ± 1.2	13.3 ± 1.1	10.1 ± 1.5	5.84 ± 0.04
SC_168	110.78108	−73.44683	9.3 ± 1.2	8.7 ± 0.7	10.2 ± 0.3	11.1 ± 1.2	6.4 ± 1.1	7.3 ± 0.4	5.98 ± 0.05
SC_169	110.80459	−73.44832	10.5 ± 1.2	10.6 ± 0.7	7.2 ± 0.6	6.7 ± 1.2	5.2 ± 0.9	1.5 ± 1.5	5.90 ± 0.05
SC_170	110.79816	−73.44769	5.8 ± 1.2	11.9 ± 0.5	10.0 ± 0.3	10.9 ± 1.0	7.9 ± 0.1	2.7 ± 1.5	5.79 ± 0.09
SC_171	110.79823	−73.44778	11.9 ± 1.2	15.5 ± 0.6	12.8 ± 0.4	10.3 ± 1.2	6.8 ± 1.1	5.0 ± 1.5	6.21 ± 0.04
SC_172	110.86482	−73.45783	3.7 ± 1.2	13.8 ± 0.6	16.7 ± 0.6	13.5 ± 1.2	6.4 ± 1.1	3.0 ± 1.5	6.65 ± 0.14
SC_173	110.86402	−73.45812	6.7 ± 1.2	10.8 ± 0.7	10.2 ± 0.5	10.1 ± 1.2	6.6 ± 0.6	6.9 ± 1.5	5.77 ± 0.09
SC_174	110.90066	−73.45376	7.9 ± 1.2	13.4 ± 0.7	12.1 ± 0.6	10.2 ± 1.0	5.4 ± 1.1	3.4 ± 0.4	6.62 ± 0.07
SC_175	110.70823	−73.47715	32.5 ± 1.2	23.8 ± 0.5	17.1 ± 0.5	19.8 ± 1.2	25.9 ± 1.1	18.0 ± 1.5	7.12 ± 0.01
SC_176	110.68084	−73.47226	18.9 ± 1.2	24.8 ± 0.6	18.8 ± 0.5	12.3 ± 0.6	10.2 ± 1.1	7.9 ± 1.5	6.89 ± 0.03
SC_177	110.64783	−73.47067	5.3 ± 1.2	10.4 ± 0.8	10.6 ± 0.6	14.5 ± 1.2	12.2 ± 1.1	8.8 ± 1.5	6.33 ± 0.09

Note. All fluxes are corrected for Galactic extinction. The errors in masses are derived from the photometry only and do not include uncertainties in the *M/L* ratio.

based forced photometry including the PSF of the observations. We first compared the one-dimensional projected light profiles from the stack of all compact star clusters to the one of the PSF (left panel of Figure 2). This test shows that the star clusters are indeed consistent with unresolved point sources, hence we use the point-source fitting option of TRACTOR. In the following, we fit the photometry of individual sources to study the variations in the stellar population across our sample. We also derive the photometry from the stacks of the sources in each of the six NIRCam filters to study the average properties. In both cases, we create cutouts of 0.″8 size of all the sources. The stacks were created by first performing a local background subtraction (measured in a sky annulus with an inner radius of 5 px and an outer radius of 10 px) on the individual cutouts and

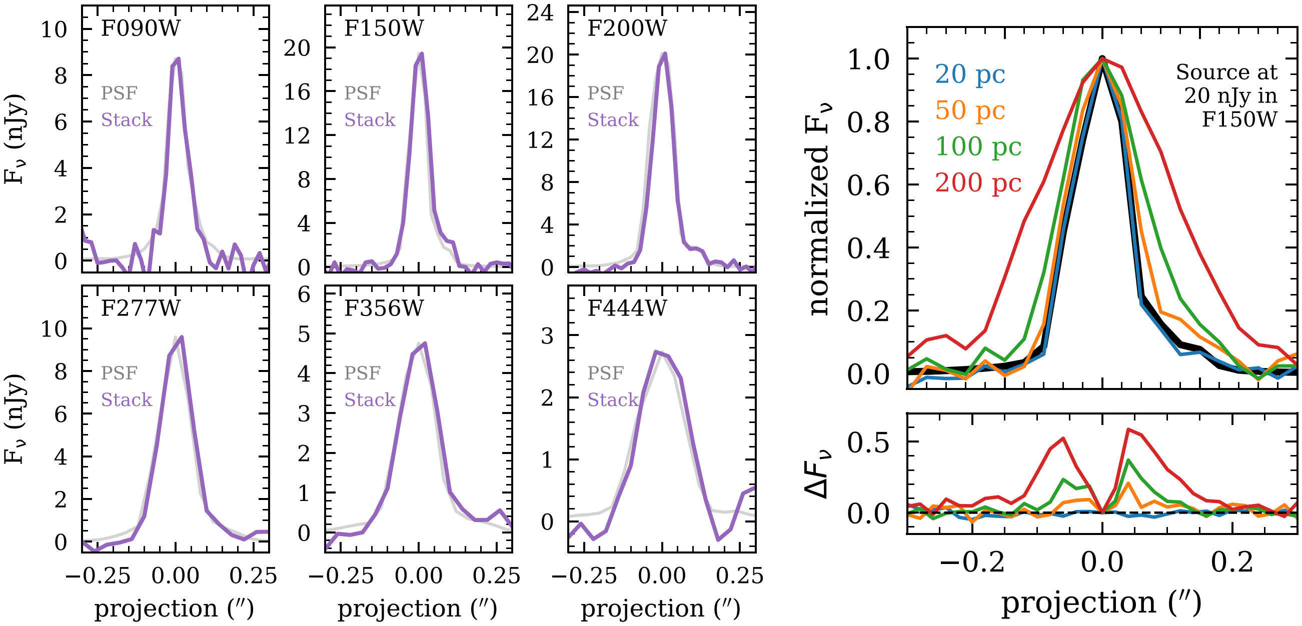

Figure 2. Left: one-dimensional light profiles of the extracted compact star clusters (purple; stacked in each filter) and the PSF (gray) in all six NIRCam filters. This shows the unresolved nature of the extracted sources. Right: simulation to assess the maximum upper limit in size of an unresolved source given the PSF in the NIRCam/F150W filter (black). We simulated sources with half-light radii of 20, 50, 100, and 200 pc (blue, orange, green, and red lines) at $z = 0.39$ and a peak flux of 20 nJy, consistent with observations of the F150W stack (see left panel). We convolved those profiles with the PSF (which is shown as the thick black line) and include realistic noise from the real observations. We find that we would be able to resolve source larger than 50 pc. Hence, the selected compact star clusters must have sizes less than 50 pc. The lower panel shows the residual (source−PSF profile).

then combining them via median stacking. The following steps are then identical for the fitting of individual sources and the stacks. TRACTOR is run on the 0.″8 cutouts applying a point-source model, using the F200W position of the sources as prior (determined from the zeroth-order moment of light on the source). During the fitting, the position is free to vary within ±2 pixels of the prior position. This helps to mitigate potential misalignments between the different image products. In addition, we let TRACTOR fit and subtract the (slowly varying on 0.″8 scales) local background at the position of the source to remove the contribution of the halo from nearby cluster galaxies and the intracluster light. Note that for that reason, simple aperture photometry will result in overestimated flux measurements. The inverse variance image (used for error estimation) is created as $1/\sigma^2$ with σ derived from σ-clipping statistics on a large region of the image not contaminated by the intracluster light and other galaxies. The variance output by TRACTOR is used to obtain the uncertainties on the flux measurements.

Figure 3 shows the fits to the stacked cutouts of the compact star clusters in the six different bands. The point-source assumption is also validated by the residuals, which are consistent with zero. The NIRCam six-band photometry derived for the stack is listed in Table 2.

2.5. Spectral Energy Distribution (SED) Fitting

To study the properties of the compact star clusters, we fit simple stellar population (SSP) models to the photometry of the median stacks obtained in Section 2.4. We assume that the star clusters have been formed in a single burst, thus are well described with an SSP model. Given the low sampling in wavelength of these data, we think that this is a good approximation as multiple stellar populations would be difficult to tell apart if they exist. Before fitting, we need to correct the extracted flux densities for Milky Way dust extinction, which we obtain from the Schlegel et al. (1998) dust maps[8] recalibrated by Schlafly & Finkbeiner (2011). The dust extinction toward the SMACS0723 is significant at an $E(B-V) \sim 0.2$ mag level, which results in a wavelength-dependent extinction of ~0.25 mag at 0.9 μm, ~0.07 mag at 2.0 μm, and less than 0.03 mag at 4.4 μm assuming the Fitzpatrick (1999) dust extinction curve. We use these values to correct the measured flux densities of the star clusters. For our fiducial SSP models, we chose "Padova 1994" stellar evolutionary tracks (Bertelli et al. 1994) together with the Basel Stellar Library (BaSeL, version 3.1; Lejeune et al. 1997, 1998; Westera & Buser 2003) complemented by the empirical STELIB library (Le Borgne et al. 2003)[9] at wavelengths blueward of 9500 Å (see Bruzual & Charlot 2003). In the following, we assume a Chabrier (2003) IMF. These fiducial SSP models were created using the software GALAXEV[10] in a grid of different ages and stellar metallicities. Specifically, the age grid ranges from 0.5 to 11 Gyr in steps of 0.5 Gyr and we use six different stellar metallicities of 0.005, 0.02, 0.2, 0.4, 1, and 2.5 $Z_\odot$. We compared the results using these fiducial models to other SSP models as well. Specifically, we compared to the MIST stellar tracks (Choi et al. 2016; Dotter 2016), based on the MESA isochrones (Paxton et al. 2011, 2013, 2015, 2018),[11] assuming a BaSeL stellar library. These additional SSP models are created using the Flexible Stellar Population Synthesis code (FSPS; Conroy et al. 2009;

---

[8] Specifically, we use the `sfdmap` Python package (https://github.com/kbarbary/sfdmap).

[9] http://svocats.cab.inta-csic.es/stelib/index.php

[10] http://www.bruzual.org/bc03/

[11] https://waps.cfa.harvard.edu/MIST/index.html

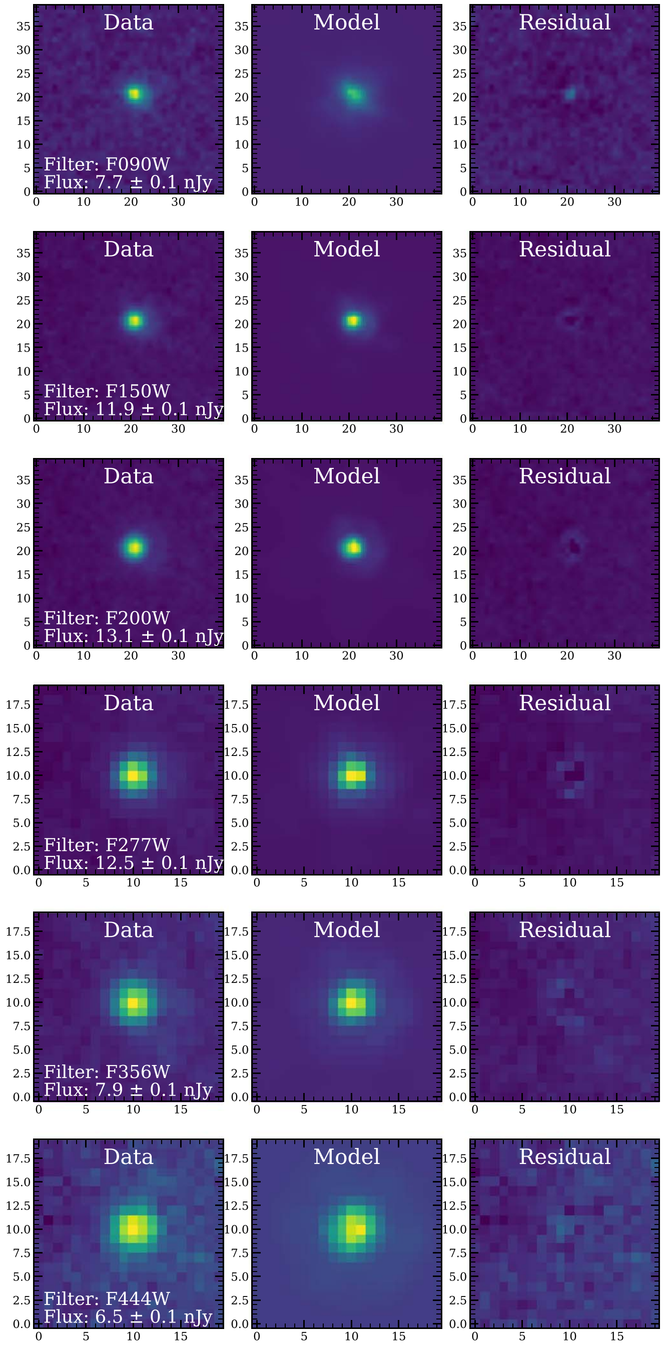

Figure 3. We use the TRACTOR software package to fit point-source profiles to the selected compact star clusters in the highly blended cluster environment. The first column shows the stacked cutouts in each of the NIRCAM band. The second and third columns show the best-fit model and the residual, respectively. The rows show the fits for the six NIRCam filters. The measured total flux values in nJy are indicated. The intensity scale is the same for each row (the residuals are consistent with zero) and all cutouts are 0$''$.8 in size.

Conroy & Gunn 2010)[12] for a Chabrier IMF and using the same age and metallicity grid. Generally, we find that wavelengths blueward of $\sim$1 μm rest frame are most affected by the choice of these different models. We will comment on the differences in the results in Section 3. The fit to the various models was performed by χ^2 minimization using the `SciPy` least-squares PYTHON package. We note that we fixed the redshift of the compact star clusters to the one of the galaxies in the SMACS0723 cluster ($z = 0.39$). In Section 3.1.1 we will show that this is indeed a good assumption based on the similarity in colors of the star clusters and galaxies at $z = 0.39$. Also, small changes in redshift (e.g., due to the kinematics in the cluster environment) do not have an impact on the fitted properties.

3. Results

3.1. Properties of Globular Clusters

3.1.1. Photometry and Colors

Figure 4 shows the observed photometric properties of the extracted compact star clusters in SMACS0723. As shown on the left panel, the brightness of the star clusters ranges from 28 to 30 mag in F090W and 27.5 to 29.5 mag in F200W (left panel). The NIRCam filters cover the (redshifted) 2 μm peak; hence, the F090W and F444W brightness is similar. The middle left panel shows the color distribution of the compact star clusters (purple circles) compared to star-forming (gray) and quiescent (red) galaxies selected in the COSMOS2020 catalog (Weaver et al. 2022) at a redshift $z = 0.39$ with $\Delta z = 0.2$[13]. Due to their SED shape, which is due to the redshifting of the 1.6 μm bump through the bandpasses, the globular clusters reside mostly at red [F090W]−[F150W] $\gtrsim 0$ colors and blue [F200W]−[F277W] $\lesssim 0$ colors. This parameter space is similar to quiescent galaxies at the same redshift, suggesting similar stellar populations. However, the star clusters are significantly fainter, 2–4 mag below the detection limits of the COSMOS surveys (right panel).

3.1.2. Population-averaged Ages and Metallicities

We note that these star clusters are faint even for JWST and most of the individual star clusters are detected at very low signal-to-noise ratio in blue and red bands where their SED flux drops. We therefore first fit SSP models (see Section 2.5) to the photometry derived from the stacked cutouts to obtain a population-averaged median age and stellar metallicity measurement. The following values for metallicity and age are therefore an average of the studied relatively massive cluster population (see also Section 3.3). Later in Section 3.2 we will fit individual star clusters to study the population variations of these properties.

Figure 5 shows the results from SED fitting using our fiducial SSP models (Padova stellar tracks) to the stacked photometry. The left panel shows a χ^2 map for the adopted age and metallicity grid with 3σ, 4σ, and 5σ contours indicated. We find a best-fit age of $1.5^{+0.5}_{-0.5}$ Gyr and a best-fit metallicity of 0.2–0.3 $Z_\odot$ (3σ). Interestingly, the χ^2 map also indicates the presence of a younger (<1 Gyr) and more metal-rich (0.4–1.0 $Z_\odot$) solution. The right panel of Figure 5 shows the data (black symbols) with the best-fit SED (black line) as well as other models (see legend in figure) for comparison with the same age or metallicity as the best fit.

The data exclude with high significance metallicities below 0.2 $Z_\odot$ as well as solar/supersolar. This is because changes in metallicity affect the colors significantly at a fixed age. For

---

[12] https://github.com/cconroy20/fsps. A Python wrapper (Johnson et al. 2021) exists at this link: https://dfm.io/python-fsps/current/.

[13] We interpolate the Suprime-Cam/z, UltraVISTA/H, UltraVISTA/K_s, and Spitzer/IRAC 3.6 μm fluxes from COSMOS2020 to obtain the corresponding fluxes in the JWST/NIRCam filters F090W, F150W, F200W, and F277W.

Table 2
Stacked Photometry for All of the Compact Star Clusters

F090W (nJy)	F150W (nJy)	F200W (nJy)	F277W (nJy)	F356W (nJy)	F444W (nJy)
9.79 ± 0.12	13.11 ± 0.07	13.98 ± 0.06	13.02 ± 0.12	8.16 ± 0.11	6.64 ± 0.15

Note. All flux densities have been corrected for Galactic extinction.

example, compare the 1.5 Gyr model at 0.02 $Z_\odot$ (gray dotted line) and at 2.5 $Z_\odot$ (gray dashed line) with the best fit (0.2 $Z_\odot$) in the right panel of Figure 5.

On the other hand, ages are not constrained well by our current data, especially with the JWST filters available. For example, ages up to 5 Gyr cannot be excluded at better than 4σ level and maximal ages of the universe at $z = 0.39$ (9.3 Gyr) are possible at 5σ level. This is expected by the lack of blue coverage of the JWST filters, and in addition the relation between color and age only changes weakly for SSPs with ages older than ∼3 Gyr. For example, the [F090W]–[F200W] color (corresponding to rest-frame $(r - H)$ color) changes by 0.4–0.6 mag (depending on metallicity) for ages <3 Gyr (caused by hot massive stars), while it only changes by ∼0.2 mag thereafter. We note that a better sampling of the observed 0.5–1.5 μm regime could constrain the older ages better (see Figure 5).

In addition, we quantify the reliability of these results by comparing to fits using the MIST isochrones as discussed in Section 2.5. We find that the models differ significantly at wavelengths blueward of ∼1 μm rest frame for low metallicities and low ages. However, we find overall that our results are robust against the choice of different model parameterizations. Specifically, using the MIST isochrones, we find consistent ages of $1.5^{+0.5}_{-0.5}$ Gyr and a best-fit metallicity of 0.4 $Z_\odot$ with a slightly larger 3σ range of 0.2–0.4 $Z_\odot$. Similarly to the other models, metallicities of <0.2 $Z_\odot$ as well as solar metallicities are robustly excluded.

3.1.3. Stellar Masses

From the best-fit SSP models obtained for each individual star cluster, we derive a V-band mass-to-light (M/L) ratio from which we can estimate the total stellar masses of the compact star clusters. For the best-fit SSP model fit to the stacked photometry, we derive a M/L ratio of 0.45 $M_\odot\, L_\odot^{-1}$. The M/L ratios of the individual star clusters range from 0.2 to 4.8 $M_\odot\, L_\odot^{-1}$. With the V-band luminosity derived from the NIRCam/F090W filter (which is close to the ∼5500 Å V-band in rest frame), we derive stellar masses for the individual star clusters and we find a median of $2.4^{+3.0}_{-1.5} \times 10^6\, M_\odot$ (using the M/L ratio derived from the stacked SED would result in a stacked median stellar mass of $3.9^{+3.2}_{-1.8} \times 10^6\, M_\odot$). As shown in the right panel in Figure 4, the star clusters line up well with quiescent galaxies at $z = 0.39$ on the K-band magnitude versus stellar mass diagram. This suggests that these compact star clusters have a similar M/L ratio as quiescent galaxies at the same redshift. Assuming the quiescent galaxy M/L relation, we would obtain an average stellar mass of $3.3^{+1.6}_{-1.1} \times 10^6\, M_\odot$.

We can compare this obtained M/L ratio to what is measured for globular clusters in the Milky Way and local galaxies. The M/L ratios depend on the age (hence mass itself) and metallicity of the stellar population. Given the estimated age and metallicity of our star clusters, we find a possible range in M/L of 1–4 $M_\odot\, L_\odot^{-1}$ in rest-frame V-band according to the observations and models in Kruijssen (2008). Note that the M/L ratio increases with age; hence, the upper end of this range would be applicable to old globular clusters, while the lower end is more common in young star clusters. Our measured M/L is consistent with younger ages.

Summarizing, the masses derived for our compact star clusters are on the high end of what is expected for globular star clusters in local galaxies (see also Figure 6). Furthermore, the high-mass end of the derived mass range may overlap with stellar masses estimated for Milky Way dwarf galaxies. To assess this, we compare the size constraints on our compact star clusters with the sizes of local dwarf galaxies.

3.1.4. Sizes

As established already in Section 2.4 and Figure 2, the selected compact star clusters are unresolved; hence, we are only able to place an upper limit on their sizes. A conservative upper limit would be the NIRCam PSF size at ∼1.5 μm, which is ∼180 pc at $z = 0.39$. To measure a more accurate upper size limit, we carry out a simple simulation as shown in the right panel of Figure 2. Specifically, we simulate point sources of different sizes (from 20 to 200 pc), which we convolve with the NIRCam/F150W PSF (Section 2.3). We add realistic background noise measured from the real NIRCam/F150W image and assume a point-source peak flux of 20 nJy, which is consistent with the one measured for the stack in the same filter (see the left panel of Figure 2). This simple simulation shows that we would be able to resolve sources larger than 50 pc. We therefore place an upper limit on the sizes of our compact star clusters of 50 pc.

Figure 6 compares this size limit to other Galactic and extragalactic sources at similar stellar masses as derived for our compact star clusters (Section 3.1.3). The sizes of the galaxies at $z = 0.39$ are taken from the HST COSMOS-DASH morphology catalog (Mowla et al. 2019; Cutler et al. 2022) in HST WFC3/F160W. At lower masses, we complement that sample with galaxies at the same redshift directly extracted from the NIRSpec/F150W image.[14] The sizes of these lower-mass galaxies are consistent with a extrapolating the M–R_e relation at $>10^9\, M_\odot$ (dashed line) to these lower masses. The galaxies are clearly more extended than the compact star clusters selected here. We also show average sizes of star-forming clumps (blue hatched area showing 1σ) in local galaxies taken from Drazinos et al. (2013) and Larson et al. (2020). At the resolution of the NIRCam observations, we would be able to marginally resolve such structures if they were present in the (quiescent) SMACS0723 host galaxies. Similarly, we would resolve objects similar in mass and size as the

---

[14] The masses and redshift are computed using the SED-fitting code EAZY (Brammer et al. 2008; Brammer 2022). Note that we only extract sources from the NIRCam field offset from the cluster's BCG to avoid the effects of lensing on the size measurements.

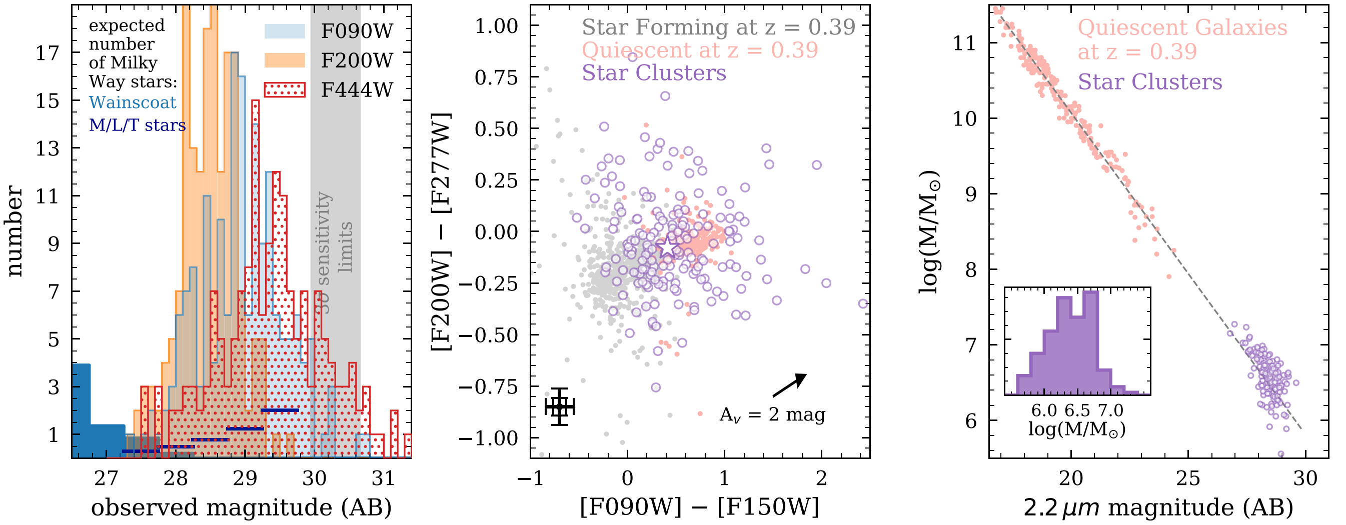

Figure 4. Properties of the compact star clusters found in the SMACS0723 field. Left panel: magnitude distribution in F090W (blue), F200W (orange), and F444W (red semifilled). The vertical gray area shows the range in 3σ limits in the three filters shown. The blue filled histogram shows the expected number of Milky Way stars from Wainscoat et al. (1992) toward the cluster field within the full NIRCam FoV. The dark blue horizontal lines show the same for the combined number of $M/L/$T stars from Kirkpatrick et al. (2021). Middle panel: the distribution of the extracted compact star clusters (purple circles; median as purple star) in color space. Typical errors in the colors are shown by the error bars in black (lowest 10% and median errors). The distribution of (dereddened) colors of star-forming (gray) and quiescent (red) galaxies at $z = 0.39$ from the COSMOS2020 catalog (Weaver et al. 2022) is shown. The star clusters match with the color distribution of the quiescent galaxy population. The $A_{\rm v} = 2$ mag extinction vector is also shown. Right panel: the 2.2 μm magnitude vs. stellar mass relation of quiescent galaxies (red dots) is similar to the one of the star clusters, indicating a similar K-band M/L ratio. The stellar masses of the star clusters (median of $2.4^{+3.0}_{-1.5} \times 10^6\,M_\odot$; see inset) are derived from the M/L ratio of the best-fit SSP models (Section 3.1.3).

Milky Way dwarf galaxies, here taken from Strigari et al. (2008).[15] We caution, however, if the dwarf galaxies have been tidally stripped in the dense cluster environment such that only the bright central core remains, we would likely not be able to distinguish those from compact star clusters. For example, a dwarf galaxy could lose more than 90% of its mass during the first few pericenter passages around its host galaxy (Ideta & Makino 2004). This would bring them to a mass consistent with our compact star clusters.

3.2. Variations in the Properties of Star Clusters

As shown in the middle panel of Figure 1, the selected compact star clusters span about 1.5–2 mag in color space, which could be indicative of variations in age and metal properties. In the following, we try to characterize these color variations in terms of variations in these physical parameters.

For this, we fit the same SSP models as described in Section 2.5 to each individual compact star cluster. We note that while the uncertainties of these measurements for individual compact star clusters are rather large due to their faintness, we still are able to investigate statistically trends of age and metallicity in our sample. Figure 7 shows the individual star clusters on the [F090W]−[F150W] versus [F200W]−[F277W] color−color diagram color-coded by the best-fit age (blue scale) and metallicity (red scale). Note that each symbol has two colors assigned (metallicity as edge-color and age as face-color). Light symbols correspond to star clusters with lower ages and metallicities, while darker symbols correspond to star clusters with older ages and higher metallicities. The background shows a Gaussian kernel density estimation (including the uncertainties of the data points) to visualize the most probable density of points. The lines indicate colors derived from the SSP models for different metallicities and ages (running from left to right, dots on lines indicate ages of 0.5, 1, 4, and 9 Gyr). Older models result in redder [F090W] −[F150W] colors, while more metal-rich models result in a reddening of both colors.

The range in colors of the individual compact star clusters are coupled with variations in ages and metallicity. This suggests different formation times and possibly different formation processes (causing different metal contents) of the star clusters in the SMACS0723 environment. We also note that the observed color (hence metallicity) distribution may be expected to be affected by the "blue tilt," caused by a lack of the most massive, metal-poor star clusters (see Forbes & Bridges 2010; Usher et al. 2018).

3.3. Comparison to Local Globular Clusters

In the following, we compare the BCG and the identified compact star clusters to systems in the local universe.

The BCG of the SMACS0723 cluster has a stellar mass of $\sim 2 \times 10^{11}\,M_\odot$ and a V-band absolute magnitude of $M_V^{Vega} \sim -23.2$,[16] which is at the faint end of the brightness distribution of the BCGs studied in Harris et al. (2014; $-24.1 \lesssim M_V^{Vega} \lesssim -23.0$). The V-band luminosities of our compact star clusters range between $2.5 \times 10^6\,L_\odot$ and $3.1 \times 10^7\,L_\odot$, which is about 1–2 orders of magnitudes brighter than the common turnover luminosity of the globular cluster luminosity function at $\sim 10^5\,L_\odot$ (Larsen et al. 2001; Harris et al. 2014). (Note that the lower limit is due to the sensitivity limit of the JWST observations.) In this luminosity range, the luminosity functions of globular clusters around local BCGs

---

[15] The masses were derived from total luminosities given in Strigari et al. (2008) and assuming the mass-to-light ratios of the galaxies measured by Revaz et al. (2009).

[16] The V-band magnitude was derived from HST photometry and subsequently converted to the Landolt V in the Vega system to be consistent with the literature.

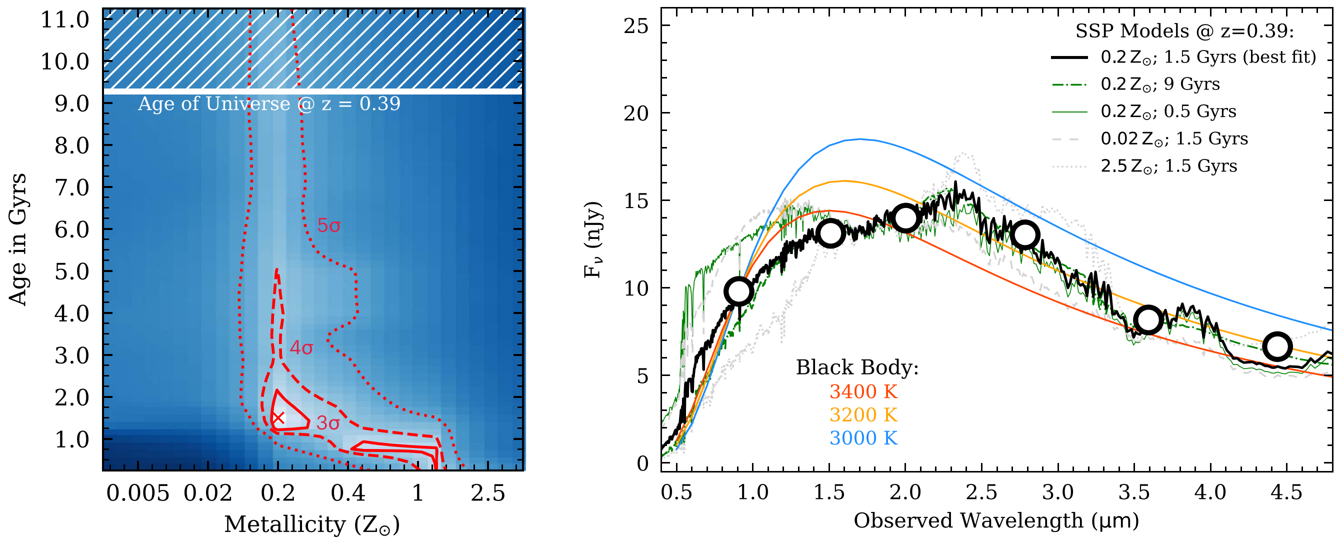

Figure 5. Results from fitting the photometry of all extracted compact star clusters. Left panel: χ^2 map of the age vs. metallicity grid with 3σ, 4σ, and 5σ contours indicated. The cross marks the best-fit solution (0.2 $Z_\odot$ and 1.5 Gyr). The age of the universe at $z = 0.39$ (9.3 Gyr) is indicated by the horizontal white line. For the full globular population we find an age of $1.5^{+0.5}_{-0.5}$ Gyr and a best-fit metallicity of 20%–30% solar. Metallicities of <20% or more than solar are ruled out at high significance. Right panel: data (black symbols) and best-fit SSP model (black line) shown with other models of different age and metallicity combinations (see legend). While different metal abundances produce different SEDs at <1.5 μm, older ages are difficult to discern. Better wavelength sampling with mediumband filters at 2–3 μm and 4–4.5 μm wavelengths would constrain older ages better. The colored lines show blackbody models at different temperatures normalized to 1 μm.

with similar luminosity find about 100 globular clusters (Harris et al. 2014), which is 60% less than what we find in the SMACS0723 cluster field. Several reasons could contribute to this difference. First, the SMACS0723 galaxy cluster is more massive ($8 \times 10^{14}\,M_\odot$ as measured by Planck) compared to the Abell clusters ($1\text{–}5 \times 10^{14}\,M_\odot$), which affects the number of globular clusters. For example, as shown in Harris et al. (2014), the luminosity function of globular clusters around the BCG in A3558 ($4.7 \times 10^{14}\,M_\odot$) peaks at 2 times higher number densities as compared to the one of the less massive cluster A1736 ($2.8 \times 10^{14}\,M_\odot$). Second, our selection includes the full ICM (over several 100 kpc; see Figure 1), which may lead to the inclusion of globular clusters around other galaxies in the vicinity of the BCG. Finally, as pointed out in Section 3.1.4, we might also include the tidally stripped compact cores of dwarf galaxies in our sample. Given the above points, the number of compact star clusters is close to what is expected based on local observations.

Note that >50% of our compact star clusters have $\log(L/L_\odot) > 6.7$ and thus would be considered as superluminous globular clusters according to Harris et al. (2014). Such superluminous objects could be related to ultracompact dwarf galaxies (or the stripped cores thereof) or bridge the gap between globular clusters and dwarf galaxies. These objects have been found in several rich local galaxy clusters (e.g., Misgeld et al. 2011; Mieske et al. 2012). SMACS0723 is a massive galaxy cluster at these redshifts (approximately a factor of 2 more massive than local galaxy clusters studied in Harris et al.); hence, the large occurrence of such superluminous globular clusters would not be surprising.

Finally, we compare the color distribution of our compact star clusters to the globular clusters around local BCGs from Harris et al. (2014). Figure 8 shows the $(B - I)_{\rm Vega}$ versus $M_I^{\rm Vega}$ color–magnitude diagram for our extracted compact star clusters at $z = 0.39$ (purple circles)[17] as well as globular clusters around the local galaxies NGC 7720 (gray) and ESO444-G046 (brown), which are the BCGs of the clusters A2634 and A3558, respectively. The former BCG is brighter (−23.8 versus −23.4 Vega mag) and resides in a more massive cluster (4.7×10^{14} versus $1.5 \times 10^{14}\,M_\odot$), which, however, is still 1.7 times less massive than SMACS0723. The compact star clusters studied in this work at $z = 0.39$ reside at the bright end of the distribution of local globular clusters. Their colors are consistent with the colors of globular clusters in A3558, the more massive one of the two local galaxy clusters shown in Figure 8. This is consistent with the idea that the brightness of the globular clusters scales with the mass of the galaxy clusters.

3.4. Comparison to Higher-redshift Globulars

Recent studies by Mowla et al. (2022) and Claeyssens et al. (2022) examined the properties of individual globular star clusters in SMACS0723 field of lensed galaxies at higher redshifts. The significant magnification (up to 100×) due to lensing allows the authors of these studies to probe fainter star clusters in the mass range of $10^5\text{–}10^7\,M_\odot$. However, the wavelength range probed by the JWST NIRCam filters is bluer due to the higher redshift of the sources, which may affect how well different properties of the clusters can be constrained with the given photometry. The Claeyssens et al. (2022) study finds relatively young ages of hundreds of Myr up to ∼1 Gyr for the studied star clusters around 18 galaxies in the redshift range $1.3 < z < 7.7$. The star clusters are consistent local globular cluster in terms of their size and stellar mass. These ages are ∼1–2 Gyr younger than what is measured for our BCG star

---

[17] These quantities have been measured on the best-fit dereddened rest-frame SSP models to the individual star clusters in the Landolt filter system (in Vega magnitudes) to be consistent with other works. Note that the JWST data does not cover the rest-frame B and I bands. Their fluxes are extrapolated from the best-fit models.

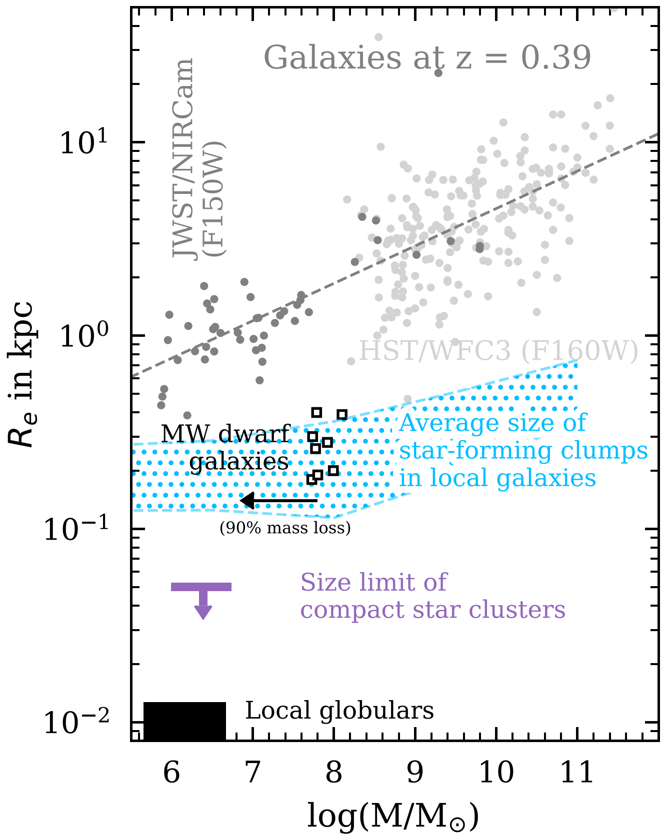

Figure 6. Upper limits on the sizes of the compact star clusters (purple) compared to sizes of $z = 0.39$ galaxies from HST COSMOS-DASH (Mowla et al. 2019; Cutler et al. 2022) in WFC3/F160W (light gray dots) and measured from NIRCam/F150W at lower masses (dark gray dots). The line shows a linear fit to the M–R_e relation. Also indicated are typical sizes of star-forming regions in local galaxies (light blue hatched with 1σ percentile; Larson et al. 2020), the sizes/masses of dwarf galaxies around the Milky Way (black squares; Strigari et al. 2008), and sizes/masses of local globular clusters (black box; Larsen et al. 2001; Hilker et al. 2020). The $z = 0.39$ compact star clusters overlap with the massive end of the stellar mass distribution of local globular cluster as well as with common masses of Milky Way dwarf assuming they lose ~90% of their mass during close passages to the BCG (black arrow).

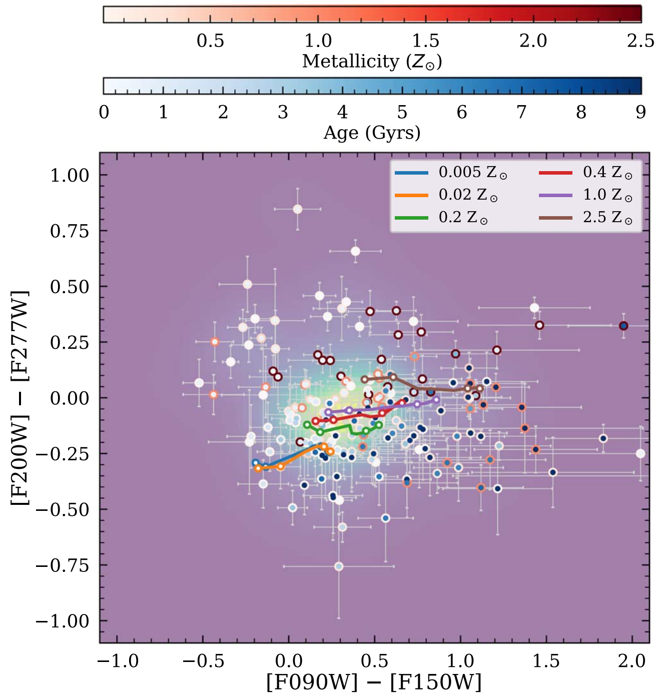

Figure 7. Individual compact clusters color-coded by their best-fit metallicity (red scale) and age (blue scale). Note that each symbol has two colors assigned (metallicity as edge-color and age as face-color). Light symbols correspond to star clusters with low ages and metallicities, while darker symbols correspond to older and more metal-rich star clusters. The background shows a Gaussian kernel density estimation of the data points for visual guidance of the density of points. The lines show models at different metallicities (color of lines) as a function of age (running from left to right, dots on lines represent ages of 0.5, 1, 4, and 9 Gyr).

clusters at 3σ, which is in line with the formation of star clusters over cosmic time. On the other hand, Mowla et al. (2022) study in detail a system dubbed as the "Sparkler" at $z = 1.378$ and find ages of 3–5 Gyr for 6 out of the 12 star clusters. This would indicate that these star clusters have been formed during the early reionization phase of the intergalactic medium at $z = 8$–11, which would be an interesting but also extreme scenario for cluster formation as understood by current models and other observations of lensed galaxies at high redshifts (see the discussion in Claeyssens et al. 2022 and references therein as well as, for example, Vanzella et al. 2017). We note that Claeyssens et al. find much younger ages (~100 Myr) for the same star clusters. Understanding this disagreement is beyond the scope of our Letter; however, there could be multiple reasons such as aperture versus PSF fitting photometer methods, the inclusion of galactic extinction, differences in SSP models and SED-fitting codes, as well as differences in the JWST photometric calibration references.

3.5. A Final Word on Milky Way Stars

Due to their pointlike nature and faintness, cool dwarf stars in our Milky Way could be mistaken as globular clusters in the $z = 0.39$ host galaxies. A significant contamination of our sample by such stars is, however, ruled out by two reasons.

First, as shown in Figure 5, blackbody models (representing cool Milky Way dwarf stars from 3000–3400 K) are not consistent with the extracted photometry of our sources. Specifically, the mid-infrared peak is redshifted consistent with the redshift of the cluster galaxies ($z = 0.39$). A combination of blackbody models (i.e., stars of different temperatures) would be necessary to explain the observed photometry. We note that due to the stacking analysis, stars of different temperatures can be combined, leading to a similar SED as the stacked photometry of the star clusters in our sample. As an additional test, we therefore compared the photometry of randomly picked star clusters to point sources (i.e., stars) at comparable faint magnitudes selected from the parallel NIRCam module off the center of SMACS0723. We find that the mid-infrared peak emission between the two samples is significantly offset (as a results of the redshift), suggesting negligible contribution of stars to the stack.

Second, the predicted number of stars in the NIRCam FoV is low compared to the selected compact star clusters. Specifically, we predicted the number of stars and brown dwarfs from the Wainscoat et al. (1992) as well as the Kirkpatrick et al. (2021) models. The former model is in good agreement with the number of stars in the COSMOS field (Scoville et al. 2007) as shown in Fajardo-Acosta et al. (2022); however, it does not include consistently M, L, and T spectral types, which start to contribute significantly at fainter magnitudes. The expected number of stars from the Wainscoat and Kirkpatrick models are

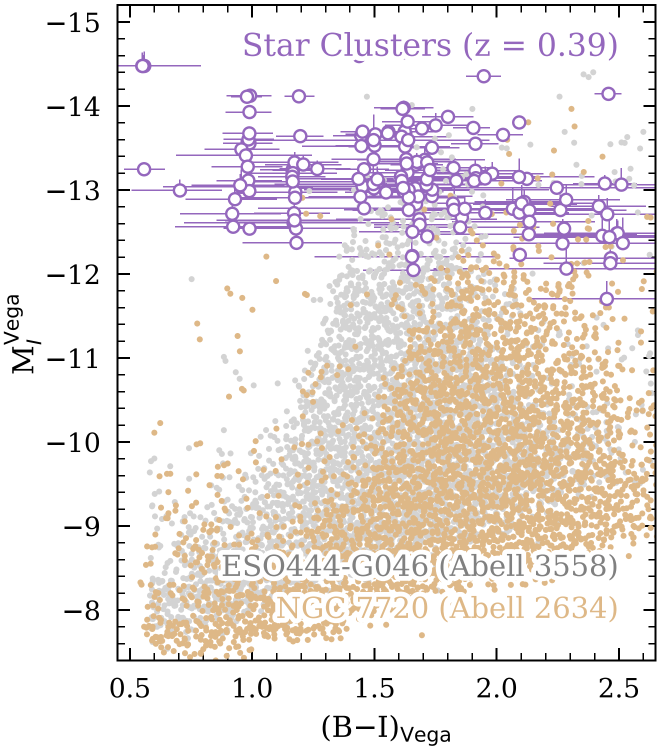

Figure 8. Color vs. magnitude diagram in $(B-I)$ vs. I-band absolute luminosity (in the Vega system). The brown and gray points correspond to the globular clusters around BCGs NGC 7720 and ESO444-G046 in the A2634 and A3558 galaxy clusters, respectively, from Harris et al. (2014). The latter galaxy cluster is 1.7 times more massive than the former but still 1.7 times less massive than SMACS0735. The compact star clusters studied in this work at $z = 0.39$ are shown as purple circles. They occupy the bright end at relatively blue $B-I$ colors consistent with the more massive of the two local galaxy clusters shown.

shown in the left panel of Figure 4 as a blue histogram and dark blue horizontal lines, respectively. We would expect on the order of ∼20 stars and dwarfs over the full FoV of NIRCam, and approximately 5 over the area where the compact star clusters are found (see Figure 1).

The negligible contribution of Milky Way stars to our sample is also suggested by comparing the number of selected star clusters in the FoVs of the two NIRCam modules. Specifically, the parallel module off-center of the SMACS0723 cluster should be dominated by Milky Way stars. Repeating the sample selection on that field results in only ∼10 point sources at similar magnitudes as the selected star clusters. Conservatively assuming that these are all stars and that the stellar density is the same in both FoVs, we would expect <10 out of the 178 selected compact star clusters to be Milky Way stars.

Vice versa, we note that globular cluster and dwarf galaxies in and around our Milky Way would be easily resolved by JWST and can therefore be ruled out.

4. Summary and Conclusions

JWST's depth and resolution provides the exciting opportunity to study the faintest and most compact star clusters in our universe. Here, we use the NIRCam early release observations of the SMACS0723 galaxy cluster at $z = 0.39$ to study a population of 178 compact star clusters residing in the intracluster region.

We extract the photometry of these point sources with the TRACTOR software using robust PSF measurements. We note that there is considerable Galactic dust extinction toward the SMACS0723 field, which needs to be corrected for. We find that the compact star clusters occupy a similar location in [F090W]−[F150W] versus [F200W]−[F277W] color space as quiescent galaxies at the same redshifts (Figure 4). However, the star clusters are more than 2–4 mag fainter than the detection limits of current wide-field surveys and have sizes that are smaller than 50 pc (Figures 2 and 6).

The photometry of the star clusters is fit with SSP models to obtain constraints on their masses, age, and stellar metallicity (Figure 5). Different stellar models are tested and the results are found to be robust under the different choices. We derive metallicities between 0.2 and 0.3 $Z_\odot$ and robustly exclude $<0.2\,Z_\odot$ and solar/supersolar metallicities at 4σ level. For the ages, we find $1.5^{+0.5}_{-0.5}$ Gyr, ruling out ages >5 Gyr at 4σ confidence. The photometry is, however, consistent with older ages up to 9 Gyr at the 5σ level, mainly due to the relatively flat relation between color and age at ages >3 Gyr. In addition, we find indications of variations of age and metallicity in this cluster population (Figure 7).

Assuming the M/L ratios of the best-fit SSP models, we derive stellar masses for the star clusters of $2.4^{+3.0}_{-1.5} \times 10^6\,M_\odot$ (Figure 4). We note that this M/L ratio is similar to the one of quiescent galaxies at the same redshift and consistent with models and observed ratios of local globular cluster. The stellar masses of our compact star clusters lie at the high-mass end of average masses of local globular cluster and there could be overlap with masses of local dwarf galaxies (Figure 6).

All in all, this suggests that these objects are likely young to middle-aged, compact star clusters (sizes <50 pc) with formation times at $z = 0.5$–0.7. Such a young age and modest metallicity support a scenario where the star clusters have been formed recently and then are stripped away several 100 kpc (projected) from their host galaxies due to the interactions in the cluster field. On the other hand, these clusters could have been formed recently in cold flows onto the cluster core (e.g., Holtzman et al. 1992). Related to this, the recent work by Lee et al. (2022) studies the spatial distribution of these star clusters and indicates that they follow closely the intercluster light and trace well the dark matter structure of the galaxy cluster. This would be more in support of a scenario in which the star clusters are stripped from their host galaxies in this highly interactive environment. A narrower sampling of the 1–5 μm wavelength with photometry or spectroscopy could help in determining more robust ages to place more stringent constraints on the formation scenario.

The star clusters probed here are 1–2 orders of magnitude brighter than the turnover of the globular cluster luminosity function measured around BCGs in local galaxy clusters. The lower end of the luminosity distribution is limited by JWST's sensitivity. At these luminosities, the clusters are in the regime of superluminous globular cluster as defined in Harris et al. (2014); however, it is important to note that SMACS0723 is relatively massive compared to local galaxy clusters (although its BCG is at the lower end of the luminosity distribution of the local BCGs probed in Harris et al.). Interestingly, the $(B-I)$ color distribution of compact star clusters in SMACS0723 is similar to the one of globular clusters in the ∼1.7× less massive A3558 cluster, one of the most massive clusters studied in that work (Figure 8).

We note that the star clusters here are, at *maximal* sizes of 50 pc and masses at the high end of local globular cluster, among the most compact stellar agglomerations (Figure 6). Compact star clusters or globular clusters are a likely explanation of these objects; however, we note that the stripped compact cores of dwarf galaxies could be an alternative explanation (see, for example, Ideta & Makino 2004 for a discussion of the origin of ω Centauri). For example, number estimates based on the Illustris simulation (Vogelsberger et al. 2014a, 2014b; Genel et al. 2014) suggest several hundreds of dwarf galaxies at masses of $10^7 M_\odot$ in clusters with $M_{200} > 5 \times 10^{13} M_\odot$, including SMACS0723 at a mass of $8.4 \times 10^{14} M_\odot$ (Mistani et al. 2016; Coe et al. 2019). Simulations suggest that a dwarf galaxy could lose $\sim$90% of its mass during the first few pericenter passages around its host galaxy (e.g., Ideta & Makino 2004), making their masses consistent with the ones measured for the clusters (Figure 6). If a fraction of the expected number of dwarf galaxies gets stripped in the cluster environment, compact cores of these dwarfs could become comparable in number with the compact star clusters seen here.

We thank Sergio Fajardo-Acosta, Alastair Edge, and Jessica Krick for fruitful discussions on the topic of stars and globular clusters. We also thank the anonymous referee for the helpful input, which significantly improved the quality of this manuscript. This research is partially funded by the Joint Survey Processing effort at IPAC/Caltech through NASA grant NNN12AA01C. This research made use of the NASA/IPAC Extragalactic Database (NED), which is operated by the Jet Propulsion Laboratory, California Institute of Technology, under contract with the National Aeronautics and Space Administration. The Cosmic Dawn Center (DAWN) is funded by the Danish National Research Foundation under grant No. 140. This work has been based on observations made with the NASA/ESA/CSA James Webb Space Telescope. The data were obtained from the Mikulski Archive for Space Telescopes at the Space Telescope Science Institute, which is operated by the Association of Universities for Research in Astronomy, Inc., under NASA contract NAS 5-03127 for JWST. These observations are associated with JWST programs 2736. The authors acknowledge the ERO teams led by Klaus M. Pontoppidan for developing their observing programs with a zero-exclusive-access period.

Facilities: JWST (NIRCam), VLT (MUSE)

Software: `astropy` (Astropy Collaboration et al. 2013, 2018), `Source Extractor` (Bertin & Arnouts 1996), `Grizli` (Brammer & Matharu 2021), `GALAXEV` (Bruzual & Charlot 2003), `EAZY` (Brammer et al. 2008), FSPS (Conroy et al. 2009; Conroy & Gunn 2010).

ORCID iDs

Andreas L. Faisst https://orcid.org/0000-0002-9382-9832
Ranga Ram Chary https://orcid.org/0000-0001-7583-0621
Gabriel Brammer https://orcid.org/0000-0003-2680-005X
Sune Toft https://orcid.org/0000-0003-3631-7176

References

Alamo-Martínez, K. A., Blakeslee, J. P., Jee, M. J., et al. 2013, ApJ, 775, 20
Astropy Collaboration, Robitaille, T. P., Tollerud, E. J., et al. 2013, A&A, 558, A33
Astropy Collaboration, Price-Whelan, A. M., Sipőcz, B. M., et al. 2018, AJ, 156, 123
Bassino, L. P., Cellone, S. A., Forte, J. C., & Dirsch, B. 2003, A&A, 399, 489
Bertelli, G., Bressan, A., Chiosi, C., Fagotto, F., & Nasi, E. 1994, A&AS, 106, 275
Bertin, E., & Arnouts, S. 1996, A&AS, 117, 393
Brammer, G. 2022, Images and catalogs of HST and JWST images in the SMACS-0723 Field, Zenodo, doi:10.5281/zenodo.6874301
Brammer, G., & Matharu, J. 2021, gbrammer/grizli: Release 2021, v1.3.2, Zenodo, doi:10.5281/zenodo.1146904
Brammer, G. B., van Dokkum, P. G., & Coppi, P. 2008, ApJ, 686, 1503
Brodie, J. P., & Strader, J. 2006, ARA&A, 44, 193
Brodie, J. P., Romanowsky, A. J., Strader, J., et al. 2014, ApJ, 796, 52
Bruzual, G., & Charlot, S. 2003, MNRAS, 344, 1000
Chabrier, G. 2003, PASP, 115, 763
Choi, J., Dotter, A., Conroy, C., et al. 2016, ApJ, 823, 102
Choksi, N., & Gnedin, O. Y. 2019, MNRAS, 488, 5409
Claeyssens, A., Adamo, A., Richard, J., et al. 2022, arXiv:2208.10450
Coe, D., Salmon, B., Bradač, M., et al. 2019, ApJ, 884, 85
Conroy, C., & Gunn, J. E. 2010, ApJ, 712, 833
Conroy, C., Gunn, J. E., & White, M. 2009, ApJ, 699, 486
Cutler, S. E., Whitaker, K. E., Mowla, L. A., et al. 2022, ApJ, 925, 34
Davidzon, I., Ilbert, O., Laigle, C., et al. 2017, A&A, 605, A70
de Grijs, R., O'Connell, R. W., & Gallagher, J. S. I. 2001, AJ, 121, 768
Dotter, A. 2016, ApJS, 222, 8
Drazinos, P., Kontizas, E., Karampelas, A., Kontizas, M., & Dapergolas, A. 2013, A&A, 553, A87
Ebeling, H., Edge, A. C., & Henry, J. P. 2001, ApJ, 553, 668
El-Badry, K., Quataert, E., Weisz, D. R., Choksi, N., & Boylan-Kolchin, M. 2019, MNRAS, 482, 4528
Faisst, A. L., Chary, R. R., Fajardo-Acosta, S., et al. 2022, ApJ, 929, 66
Fajardo-Acosta, S. B., Faisst, A., Grillmair, C. J., et al. 2022, ApJ, 930, 71
Fitzpatrick, E. L. 1999, PASP, 111, 63
Forbes, D. A., & Bridges, T. 2010, MNRAS, 404, 1203
Forbes, D. A., Pastorello, N., Romanowsky, A. J., et al. 2015, MNRAS, 452, 1045
Forbes, D. A., Bastian, N., Gieles, M., et al. 2018, RSPSA, 474, 20170616
Genel, S., Vogelsberger, M., Springel, V., et al. 2014, MNRAS, 445, 175
Georgiev, I. Y., Puzia, T. H., Goudfrooij, P., & Hilker, M. 2010, MNRAS, 406, 1967
Harris, W. E. 1991, ARA&A, 29, 543
Harris, W. E., Ciccone, S. M., Eadie, G. M., et al. 2017, ApJ, 835, 101
Harris, W. E., & Racine, R. 1979, ARA&A, 17, 241
Harris, W. E., Morningstar, W., Gnedin, O. Y., et al. 2014, ApJ, 797, 128
Hilker, M., Baumgardt, H., Sollima, A., & Bellini, A. 2020, in Star Clusters: From the Milky Way to the Early Universe, Vol. 351, ed. A. Bragaglia (Cambridge: Cambridge Univ. Press), 451
Holtzman, J. A., Faber, S. M., Shaya, E. J., et al. 1992, AJ, 103, 691
Ideta, M., & Makino, J. 2004, ApJL, 616, L107
Johnson, B., Foreman-Mackey, D., Sick, J., et al. 2021, dfm/python-fsps: python-fsps v0.4.1rc1, v0.4.1rc1, Zenodo. doi:10.5281/zenodo.4737461
Jordán, A., West, M. J., Côté, P., & Marzke, R. O. 2003, AJ, 125, 1642
Kirkpatrick, J. D., Gelino, C. R., Faherty, J. K., et al. 2021, ApJS, 253, 7
Krauss, L. M., & Chaboyer, B. 2003, Sci, 299, 65
Kruijssen, J. M. D. 2008, A&A, 486, L21
Kruijssen, J. M. D. 2015, MNRAS, 454, 1658
Kruijssen, J. M. D., Pfeffer, J. L., Reina-Campos, M., Crain, R. A., & Bastian, N. 2019, MNRAS, 486, 3180
Lang, D., Hogg, D. W., & Mykytyn, D. 2016a, The Tractor: Probabilistic Astronomical Source Detection and Measurement, Astrophysics Source Code Library, record ascl:1604.008
Lang, D., Hogg, D. W., & Schlegel, D. J. 2016b, AJ, 151, 36
Larsen, S. S., Brodie, J. P., Huchra, J. P., Forbes, D. A., & Grillmair, C. J. 2001, AJ, 121, 2974
Larson, K. L., Díaz-Santos, T., Armus, L., et al. 2020, ApJ, 888, 92
Le Borgne, J. F., Bruzual, G., Pelló, R., et al. 2003, A&A, 402, 433
Leaman, R., VandenBerg, D. A., & Mendel, J. T. 2013, MNRAS, 436, 122
Lee, M. G., Bae, J. H., & Jang, I. S. 2022, ApJL, 940, L19
Lejeune, T., Cuisinier, F., & Buser, R. 1997, A&AS, 125, 229
Lejeune, T., Cuisinier, F., & Buser, R. 1998, A&AS, 130, 65
Li, H., & Gnedin, O. Y. 2019, MNRAS, 486, 4030
Mahler, G., Jauzac, M., Richard, J., et al. 2022, arXiv:2207.07101
Marín-Franch, A., Aparicio, A., Piotto, G., et al. 2009, ApJ, 694, 1498
Massari, D., Koppelman, H. H., & Helmi, A. 2019, A&A, 630, L4
Mieske, S., Hilker, M., & Misgeld, I. 2012, A&A, 537, A3
Misgeld, I., Mieske, S., Hilker, M., et al. 2011, A&A, 531, A4

Mistani, P. A., Sales, L. V., Pillepich, A., et al. 2016, MNRAS, 455, 2323
Mowla, L. A., van Dokkum, P., Brammer, G. B., et al. 2019, ApJ, 880, 57
Mowla, L. A., Iyer, K. G., Desprez, G., et al. 2022, ApJL, 937, L35
Nardiello, D., Bedin, L. R., Burgasser, A., et al. 2022, MNRAS, 517, 484
Oke, J. B. 1974, ApJS, 27, 21
Pascale, M., Frye, B. L., Diego, J., et al. 2022, ApJL, 938, L6
Paxton, B., Bildsten, L., Dotter, A., et al. 2011, ApJS, 192, 3
Paxton, B., Cantiello, M., Arras, P., et al. 2013, ApJS, 208, 4
Paxton, B., Marchant, P., Schwab, J., et al. 2015, ApJS, 220, 15
Paxton, B., Schwab, J., Bauer, E. B., et al. 2018, ApJS, 234, 34
Peebles, P. J. E., & Dicke, R. H. 1968, ApJ, 154, 891
Peng, E. W., Jordán, A., Côté, P., et al. 2008, ApJ, 681, 197
Pfeffer, J., Kruijssen, J. M. D., Crain, R. A., & Bastian, N. 2018, MNRAS, 475, 4309
Planck Collaboration, Ade, P. A. R., Aghanim, N., et al. 2011, A&A, 536, A7
Pontoppidan, K., Blome, C., Braun, H., et al. 2022, ApJL, 936, L14
Revaz, Y., Jablonka, P., Sawala, T., et al. 2009, A&A, 501, 189
Ricotti, M., Parry, O. H., & Gnedin, N. Y. 2016, ApJ, 831, 204
Rieke, M. J., Kelly, D., & Horner, S. 2005, Proc. SPIE, 5904, 1
Rigby, J., Perrin, M., McElwain, M., et al. 2022, arXiv:2207.05632
Schlafly, E. F., & Finkbeiner, D. P. 2011, ApJ, 737, 103
Schlegel, D. J., Finkbeiner, D. P., & Davis, M. 1998, ApJ, 500, 525
Schweizer, F., & Seitzer, P. 1998, AJ, 116, 2206
Scoville, N., Aussel, H., Brusa, M., et al. 2007, ApJS, 172, 1
Strigari, L. E., Bullock, J. S., Kaplinghat, M., et al. 2008, Natur, 454, 1096
Trujillo-Gomez, S., Kruijssen, J. M. D., Reina-Campos, M., et al. 2021, MNRAS, 503, 31
Usher, C., Pfeffer, J., Bastian, N., et al. 2018, MNRAS, 480, 3279
VandenBerg, D. A., Brogaard, K., Leaman, R., & Casagrande, L. 2013, ApJ, 775, 134
Vanzella, E., Calura, F., Meneghetti, M., et al. 2017, MNRAS, 467, 4304
Vogelsberger, M., Genel, S., Springel, V., et al. 2014a, Natur, 509, 177
Vogelsberger, M., Genel, S., Springel, V., et al. 2014b, MNRAS, 444, 1518
Voges, W., Aschenbach, B., Boller, T., et al. 1999, A&A, 349, 389
Wainscoat, R. J., Cohen, M., Volk, K., Walker, H. J., & Schwartz, D. E. 1992, ApJS, 83, 111
Weaver, J. R., Kauffmann, O. B., Ilbert, O., et al. 2022, ApJS, 258, 11
Westera, P., & Buser, R. 2003, in ASP Conf. Ser. 296, New Horizons in Globular Cluster Astronomy, ed. G. Piotto et al. (San Francisco, CA: ASP), 238